SEMMELWEIS EGYETEM

DOKTORI ISKOLA

Ph.D. értekezések

2424.

KISS MÁTÉ

Klinikai neurológiai kutatások

című program

Programvezető: Dr. Kovács Tibor, egyetemi tanár

Témavezető: Dr. Kozák Lajos Rudolf, egyetemi adjunktus

Improving the Efficiency of Task-based Functional Magnetic Resonance Imaging

PhD thesis

Máté Kiss

János Szentágothai Doctoral School

Semmelweis University

Supervisor:	Lajos Rudolf Kozák, MD, Ph.D
Consultant:	Viktor Andor Gál MD, Ph.D
Official reviewers:	Attila Andics, Ph.D Krisztián Szigeti, Ph.D

Head of the Final Examination Committee:	Alán Alpár, MD, PhD, D.Sc
Members of the Final Examination Committee:	Loránd Erőss, MD, Ph.D László Négyessy, MD, Ph.D

Budapest
2020

Contents

List of abbreviations

ACR	American College of Radiology
AR	Autocorrelation
ASNR	American Society of Neuroradiology
Blipped CAIPI	Blipped-controlled aliasing in Parallel Imaging
BOLD	Blood oxygen level-dependent
CBF	Cerebral blood flow
CMRO2	Cerebral metabolic rate of oxygen
CompCor	Component Based Noise Correction
CORSICA	Correction of Structured noise using independent component analysis
CSF	Cerebrospinal fluid
EBA	Extrastriate Body Area
EPI	Echo planar imaging
FA	Flip angle
FDR	False discovery rate
FFA	Fusiform face area
FID	Free induction decay
FIX	FMRIB's ICA-based X-noiseifier
FL	Full scan length
fMRI	Functional Magnetic Resonance Imaging
FOV	Field of view
FWE	Family-wise error
FWHM	Full width at half maximum
GLM	General Linear Model
Hb	Deoxygenated haemoglobin
HbO2	Oxygenated haemoglobin
HR	Heart rate
HRF	Haemodynamic response function
ICA	Independent component analysis
LMPF	Left medial prefrontal cortex
MRI	Magnetic Resonance Imaging
MB	Multiband

NMR	Nuclear Magnetic Resonance
PCA	Principal component analysis
PCC	Posterior cingulate cortex
PPA	Parahippocampal place area
RETROICOR	Retrospective correction of physiological motion effects
RF	Radio frequency
RMPF	Right medial prefrontal cortex
RS-fMRI	Resting-state functional Magnetic Resonance Imaging
ROI	Region of Interest
RV	Respiration variation
SE	Spin echo
SIR	Simultaneous image refocusing
SMS	Simultaneous multislice imaging
SNR	Signal to noise ratio
SPM	Statistical Parametric Mapping
TE	Echo time
T-fMRI	Task-based functional Magnetic Resonance Imaging
TR	Repetition time

1. Introduction

This section presents a brief summary of the problem addressed in this work. It starts by describing the motivation and the fundamental concepts of Magnetic Resonance Imaging (MRI), functional magnetic resonance imaging (fMRI) with a focus on conventional task-based fMRI (t-fMRI) at presurgical planning and a relatively new method, simultaneous multislice imaging (SMS). In the second part of my thesis the effects of physiological artefacts (breathing and pulse) and physiological-based artefacts reduction techniques in fMRI are described.

1.1. Motivation

Functional MRI measurements became widely used tools over the last decade both in clinical practice and basic research (Kesavadas and Thomas 2008; Peck et al. 2009; Pillai 2010; Vikingstad et al. 2000; Wengenroth et al. 2011). Task based fMRI and resting-state fMRI are suitable to map cognitive functions, epileptic foci (Limotai and Mirsattari 2012) and to reveal functional characteristics of various nervous system disorders (e.g. Parkinson's disease (Kahan et al. 2014) and mild cognitive impairment(Farràs-Permanyer, Guàrdia-Olmos, and Peró-Cebollero 2015)). t-fMRI is also frequently used as a non-invasive preoperative mapping technique as it can be used to localize the eloquent primary motor, sensory, memory and language areas. It is helpful to minimize the risk of developing severe neurological deficits after surgical interventions [9] [10]. Nevertheless, there are several drawbacks regarding the application of fMRI in a clinical setting, e.g. a high demand of sustained patient cooperation during the t-fMRI examinations or long scanning time. The American College of Radiology (ACR) and the American Society of Neuroradiology (ASNR) suggest at least 120 echo planar imaging (EPI) volumes to reach high statistical values and avoid false-positive results (American Society of Functional Neuroradiology 2007). Two-dimensional simultaneous multi-slice echo planar imaging is a special MRI sequence – which also available in the clinical practice – for accelerating the acquisition. SMS uses multiband excitation pulses to collect multiple slice data simultaneously and provide increases in temporal resolution. So, e.g. multiband factor of two means that it acquires two slices simultaneously, so it doubles the number of slices to be acquired in the same repetition time (TR). Using this technique more time points are recorded, and it is well suited for improving the sensitivity of task-based and resting-state fMRI imaging.

A number of artefacts can appear during SMS reconstruction e.g. ghosting artefacts or inter-slice leakage. Sophisticated reconstruction algorithms, e.g. blipped-controlled aliasing (blipped-CAIPI) (Kawin Setsompop et al. 2012) can mitigate the problems of slice dephasing. The faster data acquisition of SMS sequences can be used to acquire more volumes, thus increasing the statistical power, while also improving resting-state fMRI based networks analysis [13] [14].

Nevertheless, there are several other types of MRI artefacts, e.g. thermal noise, susceptibility artefacts and physiological noise, which can significantly decrease the sensitivity and specificity of fMRI (Frank, Buxton, and Wong 2001; Wu, Lewin, and Duerk 1997; R. M. Birn et al. 1999).

It is well known, that the physiological noise could seriously impair the performance of analytical tools used for fMRI analysis, nevertheless only a few researcher use dedicated (model-based or data-driven) physiological correction tools (PhLEM (Verstynen and Deshpande 2011), PhysIO (Kasper et al. 2017), etc.). Nonetheless the most common physiological artefact reduction technique is the "conventional/standard" high pass filter. These easy to use toolboxes may help to improve the sensitivity and specificity of t-fMRI and rs-fMRI.

1.2. Magnetic resonance imaging: basic principles

Magnetic Resonance Imaging is an imaging technique based on the physical phenomenon of the Nuclear Magnetic Resonance (NMR) effect. MRI – thanks to its excellent spatial resolution – is widely used to investigate the structure and function of the human body. Compared with other imaging modalities it has several advantages, e.g. it does not involve exposure to ionizing radiation, there are multiple contrast mechanisms are available, even without contrast agent. These advantages make MRI the most versatile imaging technique both for in clinical applications and basic research. In addition, there are several adjustable parameters (resolution, slice thickness, receiver bandwidth, slice orientation, etc.) providing further means to optimize any given examination.

Edward Purcell and Felix Bloch were the first to use the NMR effect at spectroscopy in 1946 and they showed that certain nuclei, e.g. hydrogen, possess an intrinsic magnetic moment when placed in an external magnetic field. The quantum mechanical description of a subatomic particle such as a proton implies that it has a quantized angular

momentum, called spin. Associated with the spin there is a magnetic moment. Bloch equations describe the dynamics of the magnetic moments under the influence of an external magnetic field (Bloch, Hansen, and Packard 1946). Only the unpaired protons and neutrons have contributions to the total angular momentum of the nucleus. In consequence magnetic resonance can only be achieved in atoms with unpaired nucleons (e.g. ^{1}H, ^{13}C or ^{23}Na).

Spins align themselves to an external magnetic field B_0 in the lower energy state (Grover et al. 2015). In protons and other molecules with ½ spin, another possible position is alignment in the opposite direction, albeit this is less frequent and causes energy consumption (Fig. 1.).

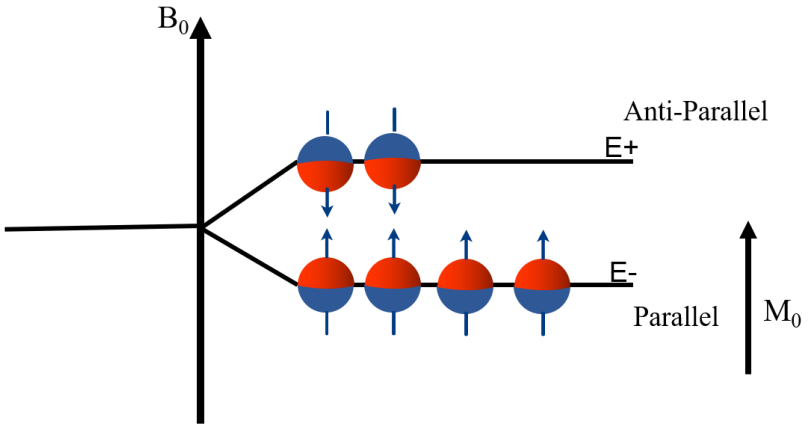

Fig 1. Spins alignment in parallel and anti-parallel direction in external magnetic field, (B_0)

The ratio between the occupation numbers of the two energy states is given by the following equation:

$$\Delta E = \gamma * \hbar * B_0 = \hbar * \mu,$$

where ν is the frequency of an electromagnetic field and μ is the Planck's constant. The spins can be treated as a macroscopic magnetization M_0. Hydrogen nuclei will provide a macroscopic magnetization when exposed to an external magnetic field, aligned in the direction of the main static field, usually referred to as the z-direction. The hydrogen protons are precessing with a dedicated frequency depending on the external magnetic field.

This precession frequency can be written with:

$$f = B_0 * \gamma,$$

where B_0 is the magnetic field strength [Tesla] and γ is the gyromagnetic ratio (γ = 42.85 MHz/T). This precessional frequency is also known as the Larmor frequency. The application of radio frequency (RF) excitation with a dedicated flip angle (α), tips the available magnetization toward a transversal plane. The resulting magnetization can be described by its remaining longitudinal component M_z along the direction of main magnetic field and a transverse component M_{xy} (Fig. 2.).

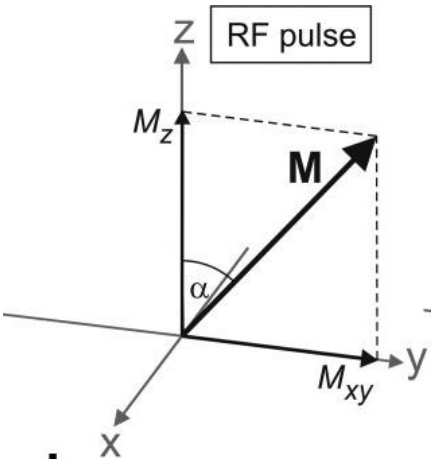

Fig 2. Spin magnetization after RF excitation (b) (Markl and Leupold 2012).

In absence of this RF pulse the hydrogen protons gradually relax back, while the phase coherence is being lost, then the transverse magnetism disappears. Individual protons relax at different rates, depending on what type of tissue the atoms are within. The precession of the protons causes an induction of current in the receiver coils of the MRI scanner. The RF pulses are repeated at a special interval, which is called time to repeat (TR).

1.3. Basic MRI pulse sequences

1.3.1. Free induction decay

Free Induction Decay (FID) is the simplest pulse sequence: with an excitation pulse (90^0), the equilibrium M_0 magnetization is displaced after the excitation, where the initial transversal magnetization is precessing with Larmor frequency. The measured signal (S) is proportional to the time derivative of the transverse magnetization and it generates a decaying harmonic signal. The decay of free induction signal is describable by T_2^* by:

$$\frac{1}{T2^*} = \frac{1}{T2'} + \frac{1}{T2},$$

where T_2' and T_2 refer to different relaxation processes. T_2 decay is the time constant that describes the decay of the transverse component of net magnetization due to accumulated phase differences caused by spin-spin interactions. T_2' is caused by local inhomogeneities in the external magnetic field, as a results spins at different locations precess at different frequencies. The dephasing – due to the different frequencies – is described by an exponential function and it causes signal loss.

1.3.2. Gradient echo sequence

One of the basic MRI sequences is the gradient echo (GRE), which uses a single RF pulse with readout gradient reversal such that the net gradient area under the curve is zero at echo time. Any gradient causes dephasing of protons. It can be easily reversed by reversing the gradient for the same length of time. The peak signal in the middle of the signal forms an echo. The readout gradient initially speeds the T2* dephasing, and it is reversed with the gradient reversal. Note, that in GRE signal loss is more rapid and thus much shorter TEs are typically used. Nevertheless, this shorter TE allows much shorter

TR, which increases T1-weighting and it allows to repeat the pulse sequence more quickly (‘MRI Physics: MRI Pulse Sequences - XRayPhysics’ n.d.). GRE is much faster, than the conventional spin echo sequence, since we do not have to wait for the rephasing after a RF pulse (Markl and Leupold 2012).

Field inhomogeneity and/or susceptibility are not focused with the gradient echo at echo time and these will influence the signal and contrast. This can be an advantage if we want to emphasize the susceptibility (e.g. iron deposition).

Fig. 3. depict a schematic representation of conventional gradient echo sequence.

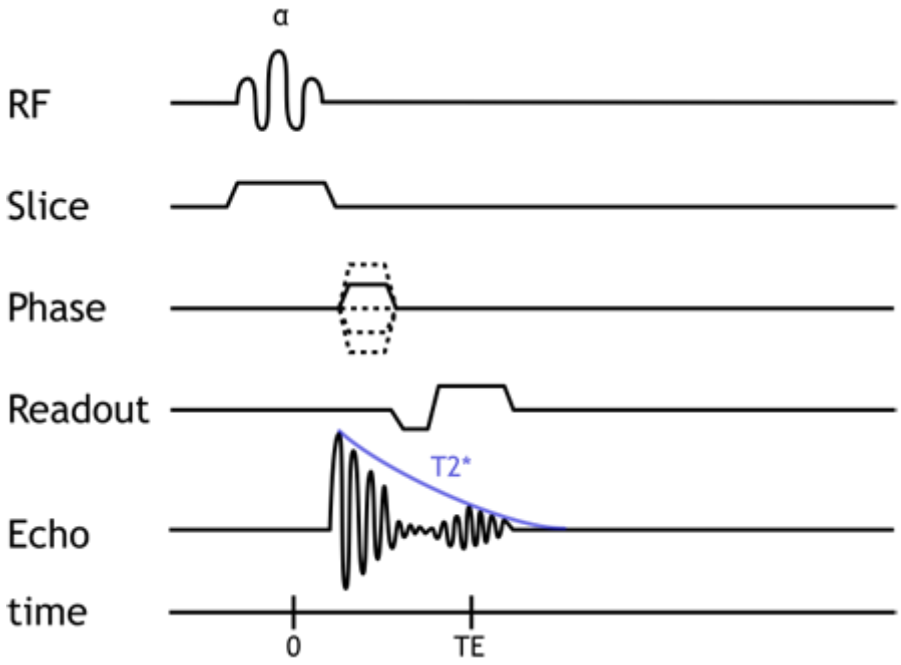

Fig. 3. Schematic depiction of the conventional gradient echo (GE) pulse sequence (‘MRI Physics: MRI Pulse Sequences - XRayPhysics’ n.d.). *Top line shows the excitation radiofrequency pulses. Slice-phase and readout lines represent the gradients, which are applied in different directions (x, y and z axes). The lower part shows the MR signal.*

1.3.3. Gradient echo EPI sequence

Nowadays, generally most fMRI is performed with Echo Planar Imaging sequence (J. E. Chen and Glover 2015), which can collect data for a two dimensional image in approximately 80-120 ms at typical resolution (3x3x3 mm^3 voxel size). EPI represented a crucial step forward in the application of MRI due to its increased speed. This increase

in speed was brought about utilising the frequency encoding gradients to form echoes by reversing their direction rapidly and using phase encoding blips to jump line by line in a k-space (Poustchi-Amin et al. 2001). The pulse diagram of an EPI sequence can be seen in Fig. 4., where G_s, G_p and G_f refer to the imaging gradients in the *x*, *y* and *z* directions. The k-space filling pattern dictated by the order, direction and magnitude of gradients is depicted in Fig 4. b. In an EPI sequence after an excitation pulse, the samples of the whole 2D k-space are acquired using a series of bipolar gradients. It leads to the sampling pattern, seen in Fig 6 b. This sampling strategy contrasts with conventional sequences, in which only one k-space line is acquired after an excitation pulse, and this sampling is much slower than in zig-zag pattern. Note, the gradient-echo EPI sequences lack the 180^0 refocusing pulse(s), echoes are created by bipolar gradients in the frequency encoding direction. The signal is measured created under the envelope of T2* relaxation. The conventional, gradient-echo EPI sequences are sensitive to susceptibility differences. This helps to detect the oxygenated differences, which provide the basis for functional MRI measurements. The major limitations of the conventional EPI sequence are geometrical distortions for the regions of large susceptibility gradients (such as facial region), limited spatial resolution and the very low bandwidth.

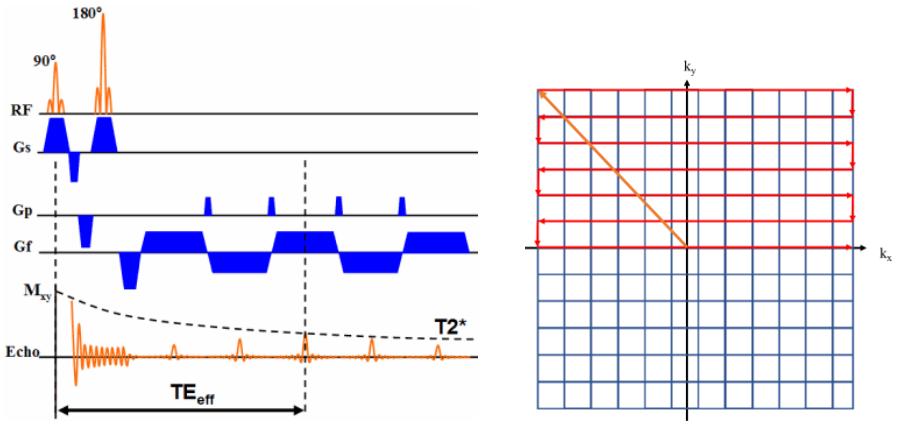

Fig. 4. Schematic depiction if the conventional 2D EPI pulse sequence ('ReviseMRI.Com : Echo Planar Imaging' n.d.). *RF means the radiofrequency excitation, Gs, Gp and Gf represent the applied gradients. The last row depicts the sampling of MR signal, where TE_{eff} is the effective echo time, which correspond to the acquisition of the middle k_y line. B. Sampling pattern (zig-zag effect) of the k-space.*

1.3.4. Simultaneous multislice imaging

Simultaneous multislice (SMS) or multiband (MB) imaging, unlike other approaches (e.g. parallel acquisition techniques) accelerates the acquisition along the slice direction using parallel image reconstruction.

Parallel imaging is a robust method for accelerating the acquisition of MRI. It works by acquiring a reduced amount of k-space data with an array of receiver coils. The number of sampled k-space lines is reduced by a factor of *n*, where *n* represents the number of missing phase encoding steps. Thereby it can significantly shorten the acquisition time. There are some limitations of parallel imaging e.g. reduced signal-to-noise ratio (SNR) and reconstruction artefacts [27] [28]. Aliased images also appear because of the undersampled data acquisition.

There are several parallel imaging algorithms that can reconstruct artefact free images:

Simultaneous acquisition of spatial harmonics (SMASH), which works in the Fourier domain uses the sensitivity profiles as basis sets to generate spatial harmonics and finally reconstruct the images (Sodickson and Manning 1997). Generalized autocalibrating partially parallel acquisition (GRAPPA) eliminates the aliased artefacts for a separate coil sensitivity calibration. In GRAPPA only a small number of k-lines are acquired (Griswold et al. 2002).

Sensitivity encoding (SENSE) is another parallel reconstruction method, which works in the image-domain. The data is first Fourier transformed, then the images are “unwarped” (eliminate the aliased image artefacts). SENSE uses the spatial information from the coil sensitivity profiles (Pruessmann et al. 1999). Controlled aliasing in parallel imaging results in higher acceleration (CAIPIRINHA) is one of the newest algorithms, which modifies the appearance of aliasing artefacts during the acquisition. It may result in an improved parallel imaging reconstruction method, multiple slices of arbitrary thickness and distance are excited simultaneously using alternative radiofrequency pulses (Breuer et al. 2005).

Parallel imaging is usually associated with a drop in SNR. In SENSE the SNR can be written with the following equation:

$$SNR = \frac{SNR}{g * \sqrt{R}},$$

where R is the acceleration factor, g is the coil geometry factor (Deshmane et al. 2012).

The above mentioned geometry factor or "g-factor" arises from the properties and geometry of the receiver coil array. It could be greater than or equal to one. If the coil sensitivities from two receiver coils are highly accelerated, the aliased pixels will in general be harder to separate which reduces the signal-to-noise ratio. The g-factor-related SNR loss from pixel to pixel and generally appears largest in the centre of the reconstructed images, where many pixels overlap, and the coil sensitivities are most similar (Deshmane et al. 2012; Glockner et al. 2005).

A significant advantage of SMS that is does not cause sensitivity reduction. SMS leads to a reduction in acquisition time by a factor of N, with no impact distortion on SNR. It became a major imaging technique during the last few years. The main benefit is an acceleration in data acquisition that is equal to the number of simultaneously excited slice. Markus Barth's review (Barth et al. 2016) give excellent and useful information about all in-slice acceleration techniques and represents several reconstruction methods. MB imaging can increase the temporal resolution in proportion to the acceleration factor, which is directly given by the number of simultaneously excited slices [34] [35]. Fig. 5. depicts a schematic representation of the SMS sequence diagram.

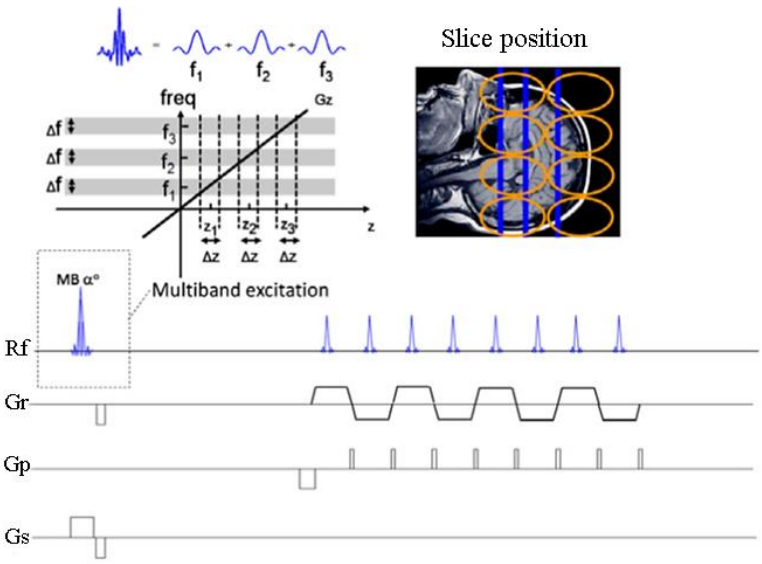

Fig. 5. SMS EPI sequence diagram. Simultaneous excitation with a multiband pulse of 3 slice plans. The signals of the slices are superimposed in the echo train and separated with different RF coils (Feinberg and Setsompop 2013).

Signal to noise ratio (SNR) decrease is much less prone to change with the acceleration factor in this case (Kawin Setsompop et al. 2012): the degradation is only related to a "g-geometry factor" and T1 relaxation effects. EPI SMS sequences are prone to N/2 Nyquist ghosting artefacts, where N is equal to the number of simultaneously excited slices. The challenge for SMS is that ghosting could not be fully corrected before unaliasing the slices, because the degree of N/2 ghosting varies by slice due to the spatial dependence of the eddy currents. Nowadays, there are several solutions, which can handle the above- mentioned problem (K. Setsompop et al. 2012; Chapman et al. 1987; Polimeni et al. 2016). Imperfect SMS reconstruction results in residual aliasing artefacts. As a result of SMS imaging, residual aliasing often arises from different slices and causes artefacts and thus is sometimes attributed as "slice leakage" (Barth et al. 2016). This artefact plays significant role especially in fMRI with EPI sequence. These residual artefacts are remarkable in the accelerated scans and they may cause false positive results.

One of the most important advantages of SMS imaging is the ability to reduce scanning durations in clinical applications like abdominal (Loenneker, Hennel, and Hennig 1996), cardiac examinations (Tong, Hocke, and Frederick 2014) or perfusion imaging [41] [42]. SMS EPI sequences are also successfully used in fMRI measurements – statistical power can increase with more measured time points. This can be done with two reconstruction methods, blipped-CAIPI or SMS with simultaneous image refocusing (SIR) (Feinberg et al. 2010; Loenneker, Hennel, and Hennig 1996; Feinberg, Reese, and Wedeen 2002; L. Chen et al. 2015). SMS-CAIPIRINHA experiments with EPI were first demonstrated by Nunes et al. (Nunes et al. 2006). The slice shift was produced by a train of unipolar gradient blips on the slice axis. This imposed the desired phase between k-space lines, but the limitation was a phase accumulation along the EPI readout that effectively dephased the spins across the slice. This was solved by Setsompop et al (Kawin Setsompop et al. 2012) with a significant modification – compared with other reconstruction methods – that uses blipped rewinder gradients which keep the phase accumulation in a dedicated range (Fig. 6). This method is widely accepted at fMRI and for diffusion weighted images.

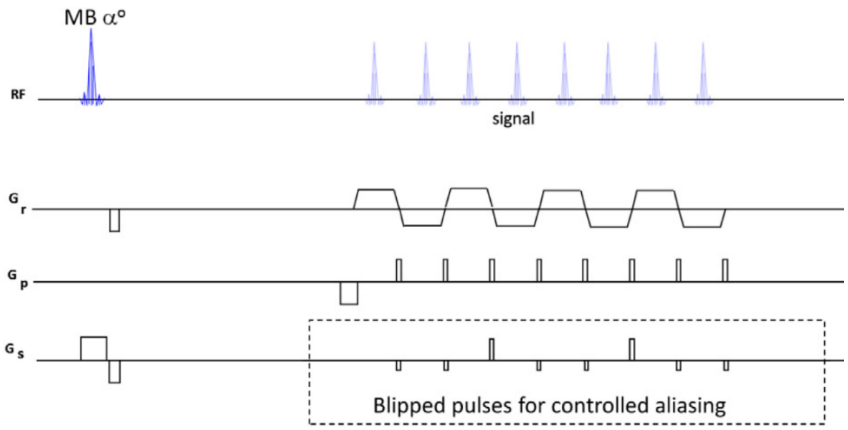

Fig. 6. SMS EPI with blipped-CAIPI reconstruction. Additional blipped gradient pulses (bottom line) added with periodic gradient moment nulling with larger amplitude phase-rewind pulses to repeatedly null the gradient moment in the echo-train (Feinberg, Reese, and Wedeen 2002).

The increase in temporal resolution allows for more advanced statistical analysis strategies, for example independent component analysis (ICA) (Smith et al. 2012), moreover physiological artefacts can be reduced more efficiently (Griffanti et al. 2014). It should be noted, that the use of very high MB factors induces higher temporal noise. Temporal noise correlations between un-aliased voxels can cause bias in resting-state fMRI.

Several studies show that the adverse effects of SMS imaging are offset by the increased amount of data points and generally higher statistical values (t-scores). Todd et al. (Todd et al. 2017) justified the SMS sequence of superior sensitivity in event related fMRI experiments: three acceleration factors and two reconstruction methods were compared with equal scanning time length. Using block designs, they concluded that increasing the acceleration up to MB factor 6 sensitivity was also increasing without any drop-in specificity. These results – the benefit of SMS acquisition – were confirmed by several other authors [48] [49]. However, considering the complexity of the acquisition and design factors, SMS technique is affecting the robustness of fMRI results (Barth et al. 2016). It is difficult to predict whether SMS-based sampling acceleration would change the required scanning time substantially to achieve a certain statistical power.

1.4. Functional magnetic resonance imaging – basic principles

Functional magnetic resonance imaging is widely used in cognitive neuroscience and presurgical planning to look for changes in neural activity that correlate with cognitive

processes. It is generally assumed that the fMRI signal is roughly proportional to a measure of the local neural activity (Logothetis et al. 2001). The relationship between the signal and the underlying neural activity depends on the fMRI acquisition technique, the stimulation protocol, etc. Functional brain mapping attempts to detect neural activity by creating contrast between active and passive (rest) conditions. All methods rely on the fact that cerebral blood flow (CBF) is increased during neural activity and it is closely connected to the neural activity [50] [51].

Since the early 1990s the Blood-oxygenation level-dependent (BOLD) signal is the dominant source of contrast in fMRI studies (Ogawa et al. 1990), where the difference between the physical properties of oxygenated and deoxygenated haemoglobin is used to create a contrast. There are two main types of fMRI: task-based and resting-state functional MRI. Task-based has also become a useful adjunct for pre-surgical planning (Petrella et al. 2006). Nevertheless, it can be associated with a high failure rate in populations that cannot comply with task paradigms. In addition, different task may be necessary to map all relevant brain functions. These limitations may be remedied or eliminated with resting-state functional MRI (rs-fMRI). This approach uses the low-frequency (<0.1 Hz) BOLD fluctuations to identify areas that are interacting at rest (Lee, Smyser, and Shimony 2013). Spontaneous fluctuations in metabolic activity are anatomically correlated within distinct functional networks (‘Functional Connectivity in the Motor Cortex of Resting Human Brain Using Echo-planar Mri - Biswal - 1995 - Magnetic Resonance in Medicine - Wiley Online Library’ n.d.). However, it does not completely replace the t-fMRI.

1.4.1. Brain metabolism and BOLD contrast

In order to understand the contrast mechanism in functional Magnetic Resonance Imaging it is necessary to be familiar with brain metabolism.

When a region of the brain is activated e.g. by a motor task (e.g. finger tapping), the neural process result a locally increased energy requirement and increased cerebral metabolic rate of oxygen (CMRO2) (Buxton and Frank 1997). This increased oxygen consumption, increases the cerebral blood flow by causing a vasomotor reaction affecting arterial sphincters, then these vessels are dilated. As a result the amount of deoxygenated haemoglobin (Hb) decreases, and the amount of oxygenated haemoglobin (HbO2) increases in the intra- and extravascular spaces locally [51] [57] (Fig. 7).

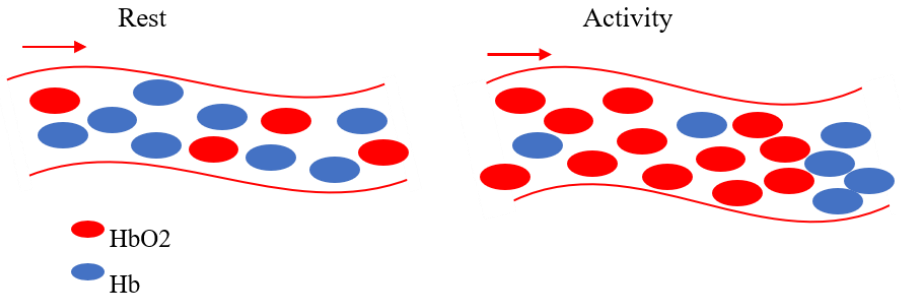

Fig. 7. Schematic representation of brain tissue containing capillary in rest phase and after neural activity. The increased blood flow causes increase in the amount of oxygenated haemoglobin (HbO2, red circles), and decrease in the amount of deoxygenated haemoglobin (Hb, blue circles).

So, there are two main consequences of increased neural activity and both can be detected with MRI: increased CBF and changes in blood oxygenation level. This change in the ratio of oxygenated and deoxygenated Hb concentration is the basis of fMRI and it is called Blood Oxygenation Level-Dependent signal or BOLD contrast. Deoxygenated haemoglobin is paramagnetic, while oxyhaemoglobin is weakly diamagnetic. Both diamagnetic and paramagnetic substances respond to externally applied magnetic field and distort its homogeneity. Paramagnetic materials increase-, and diamagnetic substances decrease the local magnetic field (Gary H. Glover 2011).

fMRI is based on the aforementioned BOLD contrast, that was first demonstrated in rats (Ogawa et al. 1990) and later in humans [26] [27]. The most widely used fMRI technique relies on T2*-weighted imaging. The T2* time constant becomes shorter in areas with low oxygenated Hb concentration and longer in areas with high oxygenated Hb concentration. The decreased deoxyhaemoglobin concentration causes more homogenous magnetic field leading to slower T2* relaxation, which can be detected as increased signal intensity on T2*-weighted images (Fig. 8).

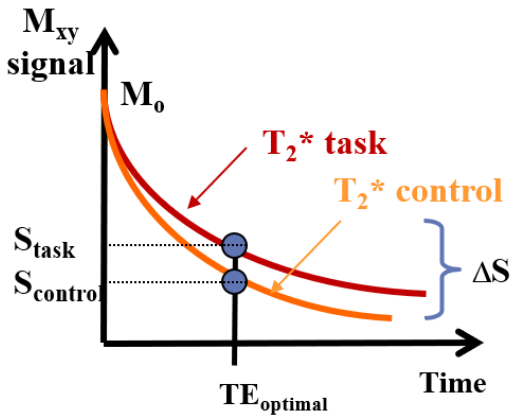

Fig. 8. T2 relaxation curves for the activated and resting phases. During brain activity (**T2* task**) the signal decays slower, therefore the signal intensity will be higher (S_{task}) compared with the rest condition (**T2* control**) and signal intensity at rest phase ($S_{control}$). The difference ΔS is measured during fMRI.*

One must note, that the BOLD signal change on T2*-weighted images does not exactly follow the neural activity, it is delayed in time. The BOLD response to a stimulus is modelled with the so-called haemodynamic response function (HRF) (Fig. 9). It may vary across different brain regions and across subjects (Handwerker, Ollinger, and D'Esposito 2004; Rangaprakash et al. 2017). Unfortunately, several factors (e.g. caffeine, drugs or medicines) affect the HRF (Diukova et al. 2012).

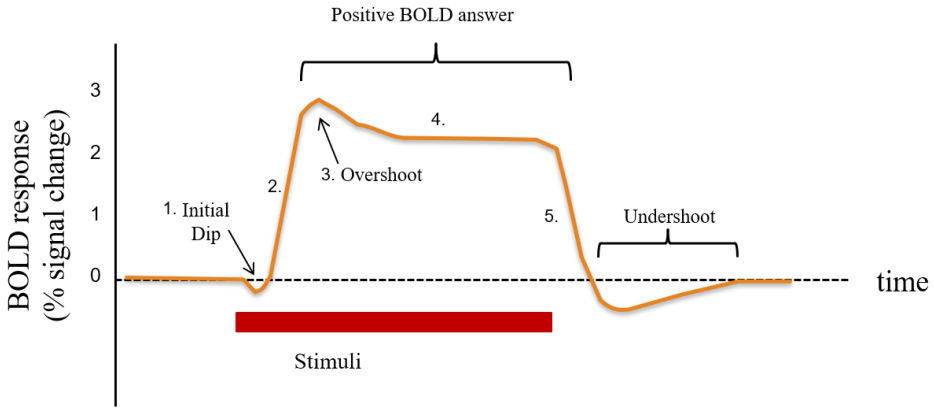

Fig. 9. BOLD response with modelled haemodynamic response function (HRF). A small BOLD signal reduction occurs immediately after the onset of neural activity, then a positive BOLD answer is detected until the end of the activity.

1.4.2. Physical basis of BOLD contrast

I described the magnetic properties of oxygenated- and deoxygenated haemoglobin in the previous chapter. Of course, brain tissues have also diamagnetic properties (due to the dominant water content). Deoxyhaemoglobin distorts the external magnetic field present in the brain and it causes more spin-spin relaxation in the surrounding tissues. T2* relaxation time in and near the vessels depends on the amount of deoxyhaemoglobin. The lower level of deoxyhaemoglobin causes slower dephasing associated with a higher T2*. Gradient echo sequences are sensitive to the T2* effects and show higher signal where blood contains more oxygenated haemoglobin.

The effects of dephasing scales with the square of magnetic field strength, therefore higher magnetic fields are more appropriate for functional MRI. Note, that these imaging sequences must be T2*-weighted. The amount of T2*-weighting is determined by the echo time.

Optimal TE value has a significant role to find the maximal signal change both for grey matter and large veins (Triantafyllou, Wald, and Hoge 2011).

1.5. Standard data processing of task-based functional MRI

The principal aim of t-fMRI data analysis is to determine cortical brain regions, where signal changes occur as a consequence of stimulation. There are three main stages of data analysis: preprocessing, statistical analysis and displaying the resulting activation maps (James et al. 2014). Multiple analysis software is available (e.g. SPM, FSL, BrainVoyager, AFNI, etc.), all of which are capable of standard preprocessing.

Slice-time correction

fMRI uses two-dimensional echo-planar imaging to collect independent slices covering the brain volume. Images are acquired sequentially at different time points during one repetition time (~2000-3000 ms). Slice scanning order also influences the delay between two consecutive slices and may add up to significant temporal shift over a whole brain volume. To compensate this effect, slice-time correction (temporal interpolation) is applied to the functional data.

Realignment – correction of head motion

Head motion could be a significant confound that can reduce the efficiency of fMRI. The aim of motion correction is to reduce movement artefacts in the fMRI time series. Most of the realignment algorithms use a reference volume and registration is usually done with a least square approach using 6 parameters rigid-body transformation, where the six parameters are estimated iteratively. Following an optimization procedure, the estimated motion parameters can be used for spatial resampling of the original, uncorrected data to match the reference.

Coregistration

It is a spatial preprocessing step that aligns functional and anatomical images in the intrasubject space. Coregistration is based on rigid-body model, albeit the cost function is mutual information. Note, that for optimal results images need to be approximately in the same orientation.

Segmentation

Segmentation is also an intrasubject step. It creates tissue probability maps for grey-, white matter and cerebrospinal fluid using a high resolution T1-weighted anatomical image.

Normalization

The main advantage of this preprocessing step – in order to make individual brain comparisons possible – to report fMRI activations within a standard anatomical space. It is especially important to organize/move brain images into the same image space if one is working on group data. During normalization images are registered to a standard space, by means of minimization of the sum of squared differences between the template image and source image (patient's brain). SPM normalization uses a 12-parameter affine transformation, e.g. to the MNI template, created from a coregistered average of 152 brain images. Of course, other templates are also available (e.g. Talairach and Tournoux).

Spatial smoothing

Functional images can be smoothed prior to the statistical analysis, to correct inter-subject spatial variability between individuals and to improve the data's compliance

with statistical assumptions. It is generally done with convolving the data with a 3D Gaussian kernel (Worsley and Friston 1995). The kernel size needs to be at least twice the voxel size for smoothing functional images (Polzehl, Voss, and Tabelow 2010). During smoothing, each voxel's intensity is changing, i.e. it will be the weighted average that incorporates the intensity values of the adjacent voxels (James et al. 2014).

Statistical analysis

The basic idea behind the GLM is the following: observed data (y) is equal to a weighted combination of several factors (x) plus an error term (ε). The equation is:

$$Y = X * \beta + \varepsilon,$$

where Y is a BOLD signal, X represents several components, which describes the observed data by means of conditions in the form of a design matrix, β represents the contribution of each component of the design matrix to the value of Y, and ε is the difference between the observed data (Y) and the predicted data (X*β).

To visualize task-related neural activity and the activated brain areas statistical tests (t-test, F-test, ANOVA, etc.) are used. SPM follows a mass univariate approach, so each voxel is analysed separately, therefore correction for multiple comparisons is required. Bonferroni, family-wise error (FWE) rate or false discovery rate (FDR) can be applied to decrease the type I. error, i.e. the number of false positive voxels.

1.6. Physiological artefacts at fMRI

Physiological noise is one of the major confounds in fMRI. It modifies the BOLD signal, resulting in extra variance of the data. It can seriously influence statistical sensitivity, resulting in false negative results (Hutton et al. 2011). Of course, false positive results may also arise when physiological noise is correlated with task timing. Resting-state fMRI results may also suffer from physiological noise, potentially leading to inaccurate functional connectivity maps (Rasmus M. Birn 2012).

The two types physiological noise relevant in fMRI analysis are those induced by the cardiac and respiratory cycles. Cardiac pulsation modulates cerebral blood flow, cerebral blood volume and also modifies the arterial pulsatility (Krüger and Glover 2001). Higher heart rate may also increase the amplitude of the arterial pulse wave and can lead

to vessel dilatation, also leading to pulsatile flow of the cerebrospinal fluid. Heart-rate variability changes local T2* values (Chang, Cunningham, and Glover 2009).

Respiration may induce modulation of the B_0 magnetic field (Raj, Anderson, and Gore 2001) and many also cause signal fluctuations: changes in respiratory volume over time modifies the concentration of blood CO_2 (Rasmus M. Birn et al. 2006), and the exhalation and inhalation induce magnetic field changes, leading to sub-voxel shifts (Windischberger et al. 2002).

The above effects cause deformation of brain tissues, indeed small displacements may appear in and around blood vessels and cerebrospinal fluid (CSF) regions (Dagli, Ingeholm, and Haxby 1999) (Lajos R. Kozák et al. 2013). MRI geometric distortions may arise from apparent movements, like the variations in air volume due to the thorax-movement induce changes in the B_0 magnetic field, which lead to signal shift in the phase-encoding direction (Raj, Anderson, and Gore 2001).

During the last decade several studies showed the relevance of physiological noise and the impact of physiological noise correction in fMRI. Most of the published studies applied noise correction to resting-state fMRI. E.g. Rasmus M. Birn et al (Rasmus M. Birn et al. 2014) compared the non-corrected rs-fMRI results with six different correction techniques and concluded that physiological corrections generally reduced the intrasubject variability while also reducing intersubject variability, thus improving test-retest reliability of estimating individual differences in functional connectivity. They also mentioned that removal of the physiological noise – arising either from cardiac pulsation or respiration – likely increase the validity of connectivity analysis.

1.7. Physiological noise correction techniques

Physiological noise correction is in general, not part of default pre-processing in task-based and resting-state fMRI data analysis. There are two main types of correction methods: data-driven (or exploratory) which rely on noise-like properties of the fMRI data and model-based, which are based on independent external measures of physiological signals. Fig. 10 depicts the types of physiological noise correction techniques.

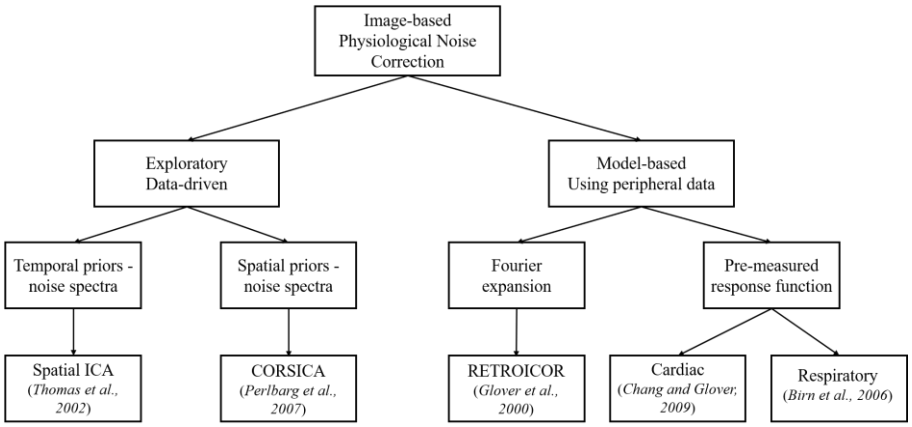

Fig. 10. Types of physiological correction techniques at fMRI

Temporal filtering is one of the most used physiological "correction method", albeit it is not as straightforward as it seems to be. Usually, in fMRI, the TR is long, which leads to under-sampling and thus potential aliasing of physiological signals (Zahneisen et al. 2014).

Principal component analysis (PCA), independent component analysis and canonical correlation analysis (CCA) are data-driven methods. An ICA decomposition can be used to detect and label several independent components as noise and reduce the negative effects of artefacts by removing these components. There are various possible ways to perform physiological noise correction: a.) using the maps' spatial information to remove specific voxels; b.) using time series data to identify and remove certain points in time (it assumes an excellent temporal resolution – unfortunately it is challenging in fMRI – due to the low temporal resolution, TR= 2 or 3 sec); c.) regressing out independent components labelled as noise from the original data (combining spatial maps with associated time series and separate the noise time series). The above-mentioned noise regression – that can be implemented in the classical general linear model (GLM analysis (Beckmann 2012)) – is the most promising approach, as it makes no assumptions about the signal of interest. ICA-based cleaning is useful in resting-state fMRI, where there is no a priori information about the signal. Thomas et al. (Thomas, Harshman, and Menon 2002) proposed a method which is based on temporal information without task related information. Perlbarg et al. used manually defined ROIs to define noise in fMRI data (Perlbarg et al. 2007). The time-series was then regressed out from the original data – it is the basis of the CORSICA (Correction of structured noise using independent component analysis) toolbox. The main advantage of

CORSICA is that it uses both spatial and temporal information and focuses on the identification of physiological noises (cardiac and respiratory fluctuations).
The common requirement – and the main drawback – of these techniques is that the user have to manually or qualitatively select or label "noise" components. Thankfully there are some toolboxes, where "noise" selection is done automatically, e.g. CompCor (Component based noise correction (Behzadi et al. 2007)), FIX (FMRIB's ICA-based X-noisifier (Salimi-Khorshidi et al. 2014)) or GIFT ('GIFT Software' n.d.). FIX extracts more than 180 features from each independent component and classifies them with dedicated classifiers namely k-nearest neighbour, support vector machine and decision tree. The GIFT toolbox extracts approximately 200 features, it uses spatial, temporal and power spectra information to separate the "noise" components from the "real" signal. Note that both FIX and GIFT concentrate not only on the physiological components – they also classify other artefacts, e.g. those which come from motion, etc. The aim of ICA-based artefact removal is to retain as much important signal as possible while removing the noisy data. Many applications of rs-fMRI, care more about keeping good signal than removing bad, particularly if the effects of residual artefacts can be ameliorated elsewhere, e.g., through the use of partial correlations in network modelling, where a move from full to partial correlation will address issues of shared confounds (Griffanti et al. 2017).

Model-based physiological correction techniques are based on modelling the different voxel-wise fluctuations recorded from peripheral electrocardiogram (ECG), photoplethysmography unit (PPU) and/or breathing belt. The first retrospective method was RETROKCOR developed by Hu et al. ('Retrospective Estimation and Correction of Physiological Fluctuation in Functional MRI - Hu - 1995 - Magnetic Resonance in Medicine - Wiley Online Library' n.d.); It fits a low-order Fourier series to the k-space time series data, and it is limited to those spatial frequencies for which the SNR is adequate to ensure a good fit of the Fourier series to the data. Glover et al. devised the RETROICOR (G. H. Glover, Li, and Ress 2000) approach which modelled the respiration and pulse phases with Fourier expansion in the image domain, it is the main difference compared to RETROKCOR. The noise from cardiac and respiratory fluctuations was found to be reduced with a greater extent using RETROICOR.
RETROICOR was later extended to model respiratory and cardiac response functions [71] [87], by applying a linear system to model respiration variation (RV) and hear rate

(HR) fluctuations. RV and HR impulse response functions are applied and deconvolved on a voxel-wise basis. The RVHR model explains a significantly greater fraction of signal variance. Removing HR and RV components from BOLD signal induce significant changes in resting-state network functional connectivities (Chang, Cunningham, and Glover 2009). Chang et al. (Chang, Cunningham, and Glover 2009) showed that RV added more variance into the BOLD signal in grey matter, while the HR component had significant effects in regions disjoint from those showing significant effects for RV, indicating differential contributions of HR and RV effects over space.

Nevertheless, there are several other models e.g non-linear Bayesian state space BOLD model (Särkkä et al. 2012), etc. but they are outside the scope of this thesis.

PhysIO toolbox (Kasper et al. 2017) is a well-documented open source software which contains the most of model-based methods, with its inputs being the peripheral recordings and its outputs being regressors representing the physiological noise components.

2. Objectives

1. The relevance of simultaneous multi-slice (SMS) EPI sequence at task-based functional MRI

Compare results obtained with a conventional EPI sequence at 0.5Hz sampling rate to those obtained with a simultaneous multi-slice sequence at 1 Hz sampling rate

Investigate the efficiency of a four-times accelerated simultaneous multi-slice (SMS) sequence. Compare the conventional EPI and SMS sequences using region of interest analysis in three pre-defined brain areas (Extrastriate Body Are- EBA; Fusiform Face Area-FFA; Parahippocampal Place Area-PPA). Determine the optimal scan length with SMS sequences, where the same- or better statistical results (t-values) are obtainable.

Compare results obtained with a conventional EPI sequence at 0.5Hz sampling rate to those obtained with a simultaneous multi-slice sequence at 2.5 Hz sampling rate

Investigate the efficiency of six times accelerated simultaneous multi-slice sequence. Compare the conventional EPI and SMS sequences with region of interest analysis at three pre-defined brain areas (Extrastriate Body Are- EBA; Fusiform Face Area-FFA; Parahippocampal Place Area-PPA). Determine the optimal scan length with SMS sequences, where the same- or better statistical results (t-values) are obtainable.

2. Role of physiological noise correction in pre-surgical functional MRI

Effects of physiological noise (breathing and pulse) on whole brain fMRI activation maps.

Compare the standard (non-corrected) and physiological artefact corrected whole brain fMRI activation maps to reveal the effects of physiological noise on fMRI mapping.

Effects of physiological noise at the eloquent brain areas in pre-surgical fMRI

Determine the role of physiological noise at the eloquent brain areas, by means of region of interest (ROI) analyses to identify differences between the non-corrected and physiological corrected maps.

3. Materials and Methods

3.1. Comparison of simultaneous multislice imaging and conventional EPI sequence

3.1.1. Subjects

21 healthy volunteers participated in this study. All participants were right-handed, without any known history of psychiatric or neurological disorders, or head injury. Every subject had normal vision and gave informed written consent in accordance with protocols approved by Health Registration and Training Centre (ENKK 006641/2016/OTIG).

3.1.2. Image acquisition

Data were acquired on a Siemens Magnetom Prisma 3T MRI scanner (Siemens Healthcare, Erlangen, Germany) at the Brain Imaging Centre, Research Centre for Natural Sciences, Hungarian Academy of Sciences. We used the standard Siemens 64-channel head-neck receiver coil. The protocol contained a T1-weighted 3D MPRAGE anatomical image (repetition time (TR)/echo time (TE)/ flip angle (FA) = 2300ms/3ms/9^0; field of view (FOV) = 256 mm; matrix size: 3x3x3.75 mm)). We used an independent functional localizer scan (TR/TE/FA: 2000ms/30ms/80^0; matrix size: 3x3x3 mm). Functional measurements were done with three different parameter sets in a balanced (across subjects) pseudo-random order: one with conventional EPI sequence using 2-fold in-plane GRAPPA acceleration (TR/TE/FA: 2000ms/30ms/79^0; matrix size: 3x3x3 mm) and another two measurements with the blipped-CAIPI Simultaneous Multislice technique (Kawin Setsompop et al. 2012) using the lack-block kernel for decreased interslice leakage [24]. We used two different acceleration factors to increase temporal resolution (Table 1. summarizes the most important scanning parameters). The total acquisition times were the same in every run of the EPI measurement.

Table 1. Scanning parameters

	Conventional EPI	SMS EPI (Acc. fact. 4)	SMS EPI (Acc. fact. 6)
TR [msec]	2000	1000	410
TE [msec]	30	30	30
FA [degree]	79	64	45
Total scan volumes acquired	336	672	1638

3.1.3. fMRI stimuli and experimental design

During the fMRI scanning session, grayscale images of human faces, houses, and headless bodies were presented. All images were equated for luminance and contrast and covered with a circular mask. We displayed all stimuli centrally, subtending 3.8 × 3.8°, on a uniform grey background via an MRI-compatible LCD screen (32’ NNL LCD Monitor, NordicNeuroLab, Bergen, Norway; refresh rate: 60 Hz) placed at 142 cm from the observer. Head motion was minimized using foam padding. Stimulus presentation was controlled by MATLAB R2015a (The MathWorks Inc., Natick, MA, USA) using PTB-3 (Brainard 1997).

The three fMRI measurements were 11 min long with different EPI sequences (Conventional EPI – MB1, SMS EPI (acceleration factor 4) – MB4, and SMS EPI (acceleration factor 6) – MB6). We randomized the order of the runs with different MB factors and counterbalanced across subjects. In each run, we used 30 seconds long periods, where faces (F), houses (H), and bodies (B) were presented in a randomized order. In each block 6 stimulus per category per block were presented. In a rest period (25 s long) only a fixation dot was presented. The first and last block was rest block and it was 30 second long. In each ~1.5 min long block, every stimulus was presented for 1 s and stimuli were separated from each other with intertrial interval (ITI) of- 2, 5, or 7 s. The order of the presentation of stimulus type (F, H, B) and ITI length was pseudorandomized for all blocks within a run and the same stimuli and design were used

for all runs and subjects. The instruction to the subjects was to view the fixation dot and pay attention to the stimuli.

We ran an independent localizer scan – without acceleration – in order to identify the relevant brain areas and select the ROIs for later analysis. During the localizer scan, which was 8.5 min (TR = 2 sec) long, a block-design paradigm was applied with 12 seconds long blocks of faces, houses and headless bodies interleaved with baseline blocks containing only a fixation dot (Hermann et al. 2017). Stimuli were presented for 500 ms with 0.5 Hz frequency. The localizer run consisted of 6 blocks of each stimulus type (F, H and B) and 19 baseline blocks, making a total number of 37 blocks, lasting 8.5 min. In order to check whether subjects paid attention to the presentation, we ran a memory task after the scanning sessions: faces, houses and bodies were presented, and subjects had to decide which of them appeared during scanning. Category-selective regions were defined based on statistical contrast maps (with $p<0.001$ threshold uncorrected) and anatomical landmarks.

3.1.4. fMRI data analysis

Standard preprocessing and analysis of the data were performed using the SPM12 toolbox (Wellcome Trust Centre for Neuroimaging, University College London, UK) and custom MATLAB codes. First, fMRI images were realigned to the first volume within a session for motion correction. Then anatomical images were co-registered to the mean functional T2* images. Thereafter segmentation and normalization to the MNI-152 space was performed with the SPM segmentation toolbox. Grey matter masks were used to restrict statistical analysis of the functional data. A 128 sec high-pass filter was used in order to remove low-frequency signal drifts. We spatially smoothed the functional data with a Gaussian kernel of 6 mm full width at half maximum. Stimulus onsets were modelled, convolved with canonical HRF and analysed with GLM. The design matrix also contained the movement-related regressors calculated by the motion correction procedure to account for movement-related variance. We calculated voxelwise contrasts (t-scores) to determine differences in the evoked BOLD signals between different stimulus conditions (e.g. face vs. houses) for the definition of the relevant ROIs using the independent functional localizer scans. Finally, within the functionally defined regions similar contrast statistics were assessed using the data acquired with different MB factors during the main experiments: mean t-scores –

reflecting the stimuli contrast statistics – within a 6 mm radius sphere centred at the peak voxel of the defined ROIs were averaged across hemispheres and used in the comparisons.

3.1.5. ROI selection for data analysis

Category-selective regions were defined based on statistical maps (with $p<0.001$ threshold uncorrected) and anatomical images – using the independent functional localizer scans. The fusiform face area (FFA (Kanwisher, McDermott, and Chun 1997)) in the mid-fusiform gyrus was identified as an area responding more strongly to faces than houses. The parahippocampal place area (PPA (Epstein and Kanwisher 1998)) in the parahippocampal gyrus was determined as the area showing significantly stronger activation to houses than faces, while the extrastriate body area (EBA (Downing 2001)) localized in the lateral occipital cortex was determined as the area responding more intensely to human bodies relative to houses. It was possible to define right FFA in 19, and left FFA in 21 subjects (average MNI coordinates ± SD: right FFA: *41.22 ± 4.23; -46 ± 6.45; -18.33 ± 4.13*. left FFA: *-40.44 ± 2.87; -50.77 ± 6.79; -20 ± 3.14*), while right PPA was found in 20 and left PPA was found in 19 subjects (right PPA: *26.22 ± 3.2; -46.33 ± 4.76; -9.33 ± 2.37*. left PPA: *-26.33 ± 2.93; -47.44 ± 3.74; -8.11 ± 2.69*). Right EBA could be defined in 21 and left EBA in 20 participants (right EBA: *49.55 ± 3.18; -71.33 ± 4.39; 4.55 ± 4.98*. left EBA: *-48.22 ± 3.2; -73.88 ± 6.63; 5.44 ± 5.39*). Fig. 11. shows example activation maps of the three relevant ROIs (FFA, PPA and EBA). Unfortunately, some ROIs, especially FFA in the visual cortex were functionally undefinable in some subjects despite using the appropriate fMRI contrast (e.g. face>non-face object stimuli for the FFA localization). One possible reason is the lower signal-to-noise characteristics (susceptibility effects) and/or lower functional specificity of these regions (Rossion et al. 2015). Naturally, participants with missing ROIs were excluded from any given analysis.

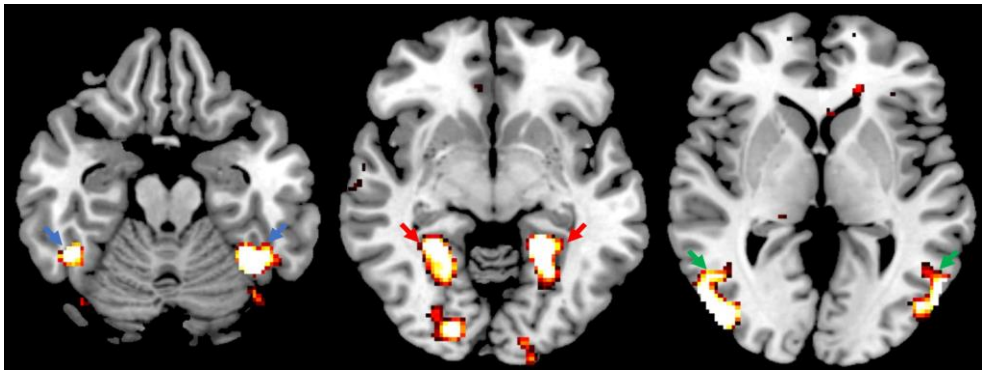

Fig.11. Typical fMRI activations of EBA (blue arrows), FFA (red arrows) and PPA (green arrows).

We also selected brain regions where we did not expect activations – these were not relevant in the stimulation paradigm. The reason was to compare the false positive rate (the fMRI specificity) of the statistics among the different acquisition rates (MB factors). Two ROIs were selected, in association with the default mode network (Meszlényi et al. 2017): posterior cingulate cortex (PCC, MNI coordinates: -3, -36, 39); left and right medial prefrontal cortices (lMPF and rMPF MNI coordinates: -3, 44, -2; 2, 57, 24). These sites are excellent for testing the specificity (Sahib et al. 2016) given that they can generate confounding neural background activity, increasing the probability of false positive statistics.

3.1.6. Comparison of the statistical power of different combinations of scan length and sampling rates

We truncated the acquired data at 4 different time points to get activity time-courses with 4 different lengths. The durations of the resulting time-courses were 124, 254, 384 and 515 seconds long, containing the initial 30 seconds rest period and 1, 2, 3 or 4 stimulus blocks respectively. We used the following consistent notations: 1/5FL, 2/5FL, 3/5FL and 4/5FL representing the approximate duration ratio relative to the non-truncated full scan length (FL).

We also truncated data acquired with MB4 and MB6, then compared the shortened scans with the full-length 11 mins standard (TR=2sec) scans to establish the efficiency of the acceleration technique and reveal the accidental differences.

ROI analysis were performed both in the relevant and irrelevant regions. We examined how the increased sampling rate affected the activation statistics – we compared the full

scan length non-accelerated sequence to truncated and full scan length MB measurements. We found significant increase/decrease in t-values in ROI analysis, where we probed the null-hypothesis whether statistical values (t-scores) based on shortened MB4 and MB6 data chunks are equal to those obtained on full-length MB1 scans, against the alternative that they are significantly different.

3.2. Physiological artefact correction for pre-surgical language fMRI

3.2.1. Subjects

14 patients with primary brain tumour participated in this study. Six female and eight male patients' (mean ± std age = 48.85 ± 9.11) data were analysed retrospectively after the fMRI examination. We mapped the primary language and motor areas. Tables 2. and 3. contain all relevant information regarding the patients. Every subject had normal vision and gave informed written consent.

3.2.2. Image acquisition

All data were acquired on a Siemens Magnetom Verio 3T scanner (Siemens Healthcare, Erlangen, Germany) at the National Institute of Clinical Neurosciences, Department of Neuroradiology. We used the standard Siemens 12-channels head receiver coil. The protocol included a T1-weighted 3D MPRAGE anatomical series (TR/TE/FA: 2300ms/2ms/9^0), FOV = 256x256 mm, slice thickness was 3mm, the slice order was interleaved. 2D EPI sequences were used to perform functional measurements with GRAPPA parallel imaging, with the following parameters: TR/TE/FA: 3000ms/30ms/90^0.

Physiological parameters (breathing and pulse) were recorded with the built-in MRI compatible devices.

3.2.3. fMRI stimuli

We used 4 different language fMRI tasks (picture naming, synonym task, auditory decision and speech comprehension) in order to map the eloquent brain areas. Every paradigm contained 6 active and 6 passive blocks, every block was 24 seconds long. Here, we give a short description about the paradigms (see Fig. 12. for a schematic

representation) (L.R. Kozák et al. 2011; Lajos Rudolf Kozák et al. 2009; Hegyi et al. 2009).

Picture naming: active condition (24s): covert naming of images presented in every 3s and decision whether the image shows a living entity or an object; passive condition (24s): Fourier-scrambled versions of images are shown, the patient is instructed to rest, but mark the direction of arrows overlaid on the images.

Synonym: active condition (24s): synonym decision making on word pairs presented at every 3s; passive condition (24s): similarity decision making on 5-letter consonant string pairs presented every 3s.

Speech comprehension: active condition (24s): listening to pre-recorded speech; passive condition (24s): listening to pre-recorded reverse speech.

Auditory decision: active condition (24s): auditory word vs. false-word decision based on presented every 3s; passive condition (24s): tone similarity decision on stimulus pairs presented every 3s.

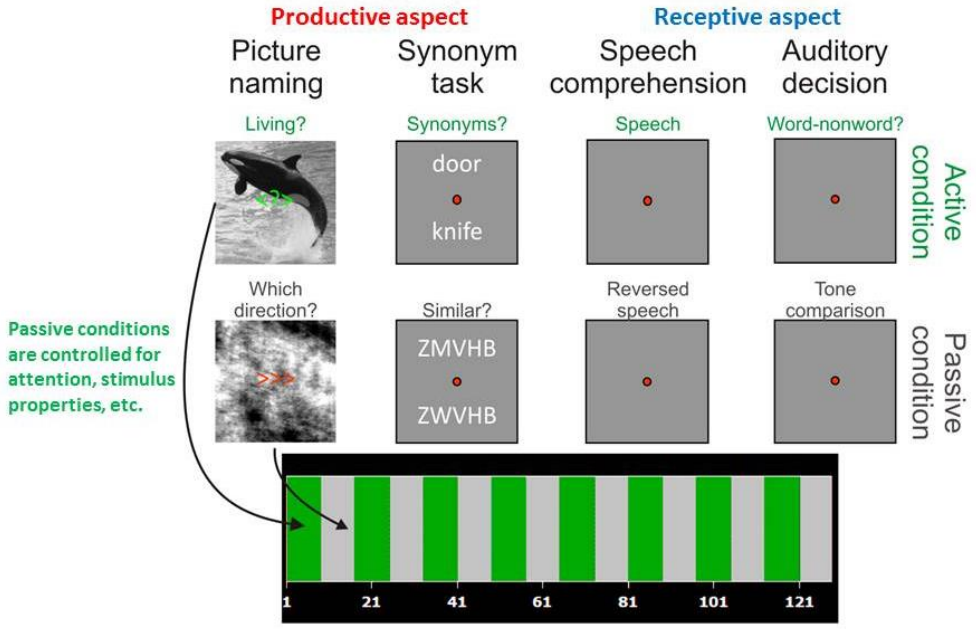

Fig. 12. Schematic representation of the applied fMRI language paradigms

Visual stimuli were displayed centrally, subtending 3.8 × 3.8°, on a uniform grey background via an MRI-compatible LCD screen (32' NNL LCD Monitor, NordicNeuroLab, Bergen, Norway; refresh rate: 60 Hz) placed at 142 cm from the observer. Head motion was minimized using foam padding. Stimulus presentation was controlled by nordicAktiva (NordicNeuroLab, Bergen, Norway) software.

3.2.4. fMRI data analysis

Standard preprocessing and analysis of the data were performed using the SPM12 toolbox (Wellcome Trust Centre for Neuroimaging, University College London, UK) and custom MATLAB (The Mathworks) codes. The fMRI volumes were realigned to the first volume within a session for motion correction. Then high-resolution anatomical images were co-registered to the mean functional T2* images. A high-pass filter (128 sec) was applied to remove low-frequency signal drifts, then spatial smoothing with a 3D Gaussian kernel of 6 mm full width at half maximum was applied. Stimulus blocks were modelled, convolved with canonical HRF and analysed within a general linear model framework. The design matrix also contained the movement-related regressors calculated by the motion correction procedure to account for movement-related variance. Voxelwise contrasts (t-scores) were calculated to assess differences in the evoked BOLD signals between different stimulus conditions (active vs. passive). We applied voxel-based threshold ($p < 0.001$), without multiple comparison correction. MRIcroGL ('Home | MRIcroGL | University of South Carolina' n.d.) was used to visualize our results.

In order to decrease the physiological artefacts we used the convolution based RETROICOR/RVHR, which identifies and eliminates breathing and pulse related artefacts (Chang, Cunningham, and Glover 2009; Chang and Glover 2009).

Task-based fMRI were analysed both with and without RETROICOR/RVHR. The Jaccard coefficient was used to quantitatively compare the activation maps obtain with and without physiological artefact correction:

$$J(A,B) = \frac{|A \cup B|}{|A \cap B|},$$

where A = standard activation map (without physiological correction), B = physiologically corrected activation map. fMRI activation maps were thresholded at $p<0.001$. If the two activation maps were same or almost the same, the Jaccard coefficient would be around 1, else it would converge to 0. We also determined the number of activated voxels ($p < 0.001$) in both activation maps and two sample t-test

was applied to reveal the significant differences. We also counted the number of non-significant voxels and determined the differences with t-test.

3.2.5. ROI selection for detailed analysis

We performed Region of Interest analysis by placing ROIs in the relevant eloquent brain areas (Broca-, Wernicke- and primary sensory-motor areas). Peak voxels were selected, and 20 mm sphere ROIs were used to extract means and standard deviations of t-values. ROI extraction was performed both on non-corrected and physiological corrected maps. Paired t-test was applied to determine the significant differences between ROIs. Levene's test (Begg 1988) was used to reveal the homogeneity of the ROIs' variance.

We also analysed the fMRI activations' extensions in the eloquent brain areas (number of voxels in an eloquent brain area activated at the significance level of $p_{uncorrected} < 0.001$). We used two-sample t-test to determine the differences between the ROIs' extensions.

4. Results

4.1. Comparison of simultaneous multislice imaging and conventional EPI sequence

4.1.1. Results of the ROI analysis: task-relevant regions

In order to reveal the significant differences between SMS EPI and conventional EPI sequences and to compare the FL measurements with truncated sequences, we assessed mean t-scores for each subject, ROI, MB factor, and truncation length. Group averages were calculated, and the mean t-scores are depicted with bar charts in Fig. 13, Fig. 14 and Fig. 15. We found significant ($p < 0.0014$) differences in the PPA ROI analysis, when compared 4/5FL and FL measurements in the case of MB4 with MB1 FL values (Fig. 15.a.). We also found significant differences ($p < 0.0056$) in EBA ROI analysis, when compared to 4/5FL and FL measurements with MB1 t-values (Fig. 13.a.).

We found non-significant differences ($p > 0.09$) – in EBA ROI analysis – between the full scan length MB1 and the extremely truncated MB4 sequences (1/5FL, 2/5FL), see Fig. 15.a. Note, that a substantial decrease in t-scores ($p < 0.001$) are detected when compared the full scan length MB1 measurement with MB4 sequence, when only 20% (1/5FL) of the full scan time was used (Fig. 13.a. first two bar charts).

We did not recognize any significant differences at any truncated scan length in the FFA ($p > 0.18$) when the acceleration factor was 4.

The multiband sequence with acceleration factor of 6 definitely overperformed the full scan length MB1 measurements in all ROIs when we used at least 60% (3/5FL) of the total scan length ($p < 0.001$).

In the FFA (Fig 14.) and EBA (Fig. 13) regions multiband measurements with acceleration factor of 6 even at 2/5FL reached significantly higher t-scores compare to FL, non-accelerated measurement ($p < 0.008$ for FFA and EBA).

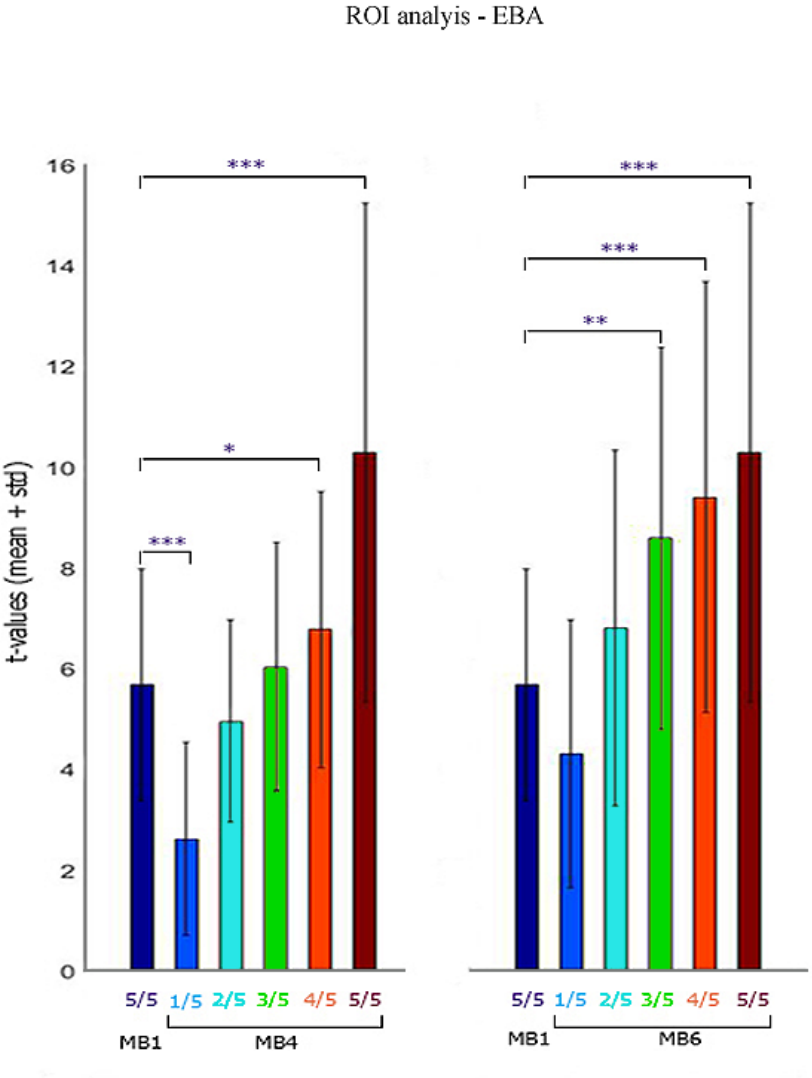

Fig.13. EBA sensitivity profile: across subject average of the t-scores. Mean ± standard deviations of the t-scores are depicted. Full-length scan time with standard (MB1) measurements (dark blue charts) are compared with the 20%, 40%, 60%, 80% and 100% of the total scan time with acceleration factors 4 (MB4) and 6 (MB6).

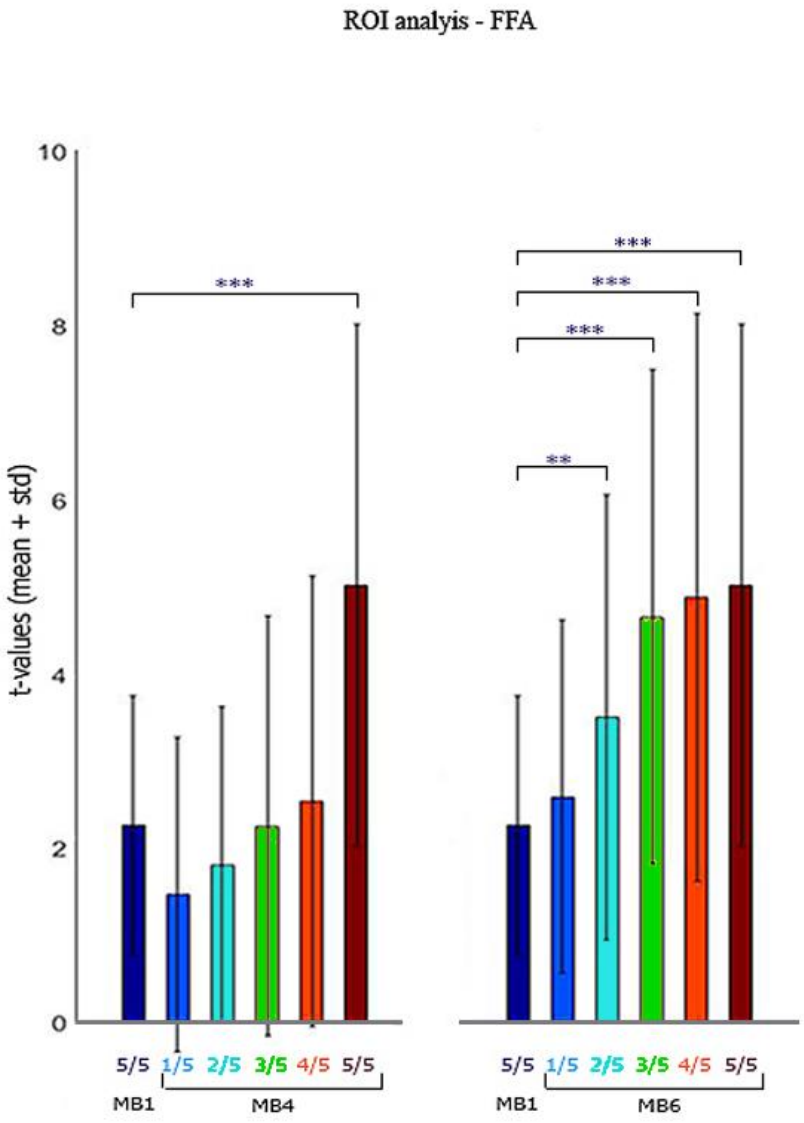

Fig.14. FFA sensitivity profile: across subject average of the t-scores. Mean ± standard deviations of the t-scores are depicted. Full-length scan time with standard (MB1) measurements (dark blue charts) are compared with the 20%, 40%, 60%, 80% and 100% of the total scan time with acceleration factors 4 (MB4) and 6 (MB6).

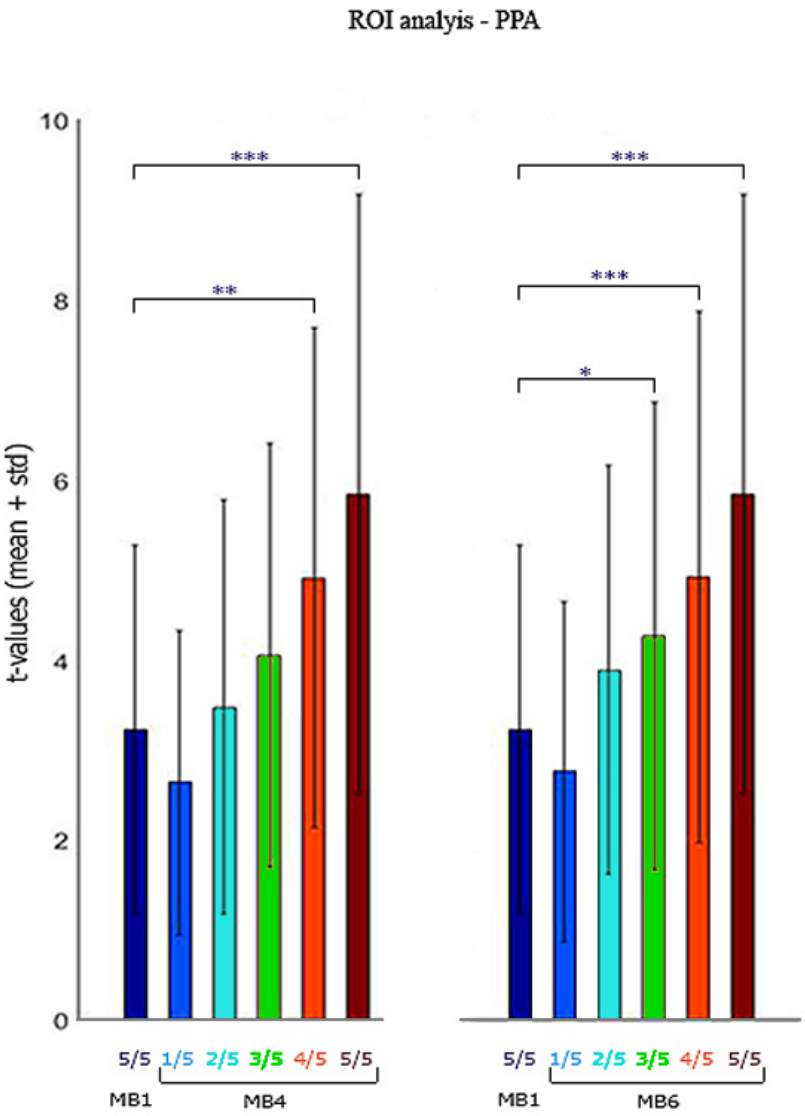

Fig.15. PPA sensitivity profile: across subject average of the t-scores. Mean ± standard deviations of the t-scores are depicted. Full-length scan time with standard (MB1) measurements (dark blue charts) are compared with the 20%, 40%, 60%, 80% and 100% of the total scan time with acceleration factors 4 (MB4) and 6 (MB6).

In order to demonstrate the performance of multiband sequences with respect to clinical practice, we show an example at a single subject level. Single subject statistical maps (thresholded at the same level, t=5) are depicted in Fig. 16. for MB4 and in Fig. 17. for MB6 measurements. Bilateral FFA can be identified at all accelerations and scan lengths (MB1 full scan length, see Fig. 16.a. and truncated MB4 scans, see Fig. 16.b.-f.). Interestingly activated areas show almost the same extent with 1/5FL (Fig. 16. b.) and

2/5FL (Fig. 16. c.) for MB4 scans. We identified stronger activations for longer measurements and the extent of activations were also larger (Fig.16. d-f.).

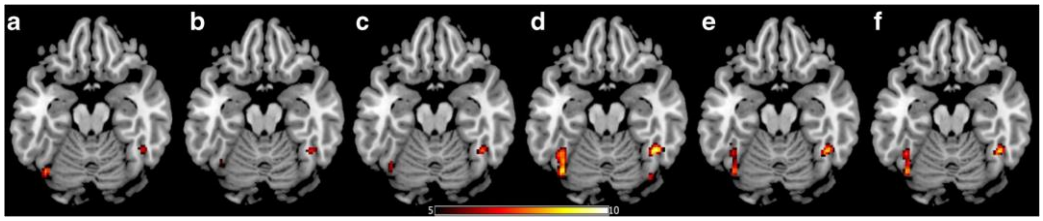

Fig. 16. Whole brain contrast maps from Volunteer 15, MB4. Bilateral fusiform face areas are identified based on ~11 min scanning with conventional EPI sequence (a.). The areas show up using multiband sequences with acceleration factor 4 and different scanning durations: 1/5FL (b), 2/5FL (c), 3/5FL (d) 4/5FL (e) and full scan length (f.). Each t-map is thresholded at the same score (t>5).

We used the same single subject t-maps (Fig. 17.) to demonstrate the MB6 measurements' efficiency with respect to acquisition length. Fusiform face area (FFA) is displayed in both hemispheres. Compared with the MB4 sequences (Fig. 16.) one must note, that the activations are more robust than the conventional MB1 and MB4 scans. More robust activations are already detected after 2 minutes of scan time (1/5FL) MB6 (Fig 17. b.).

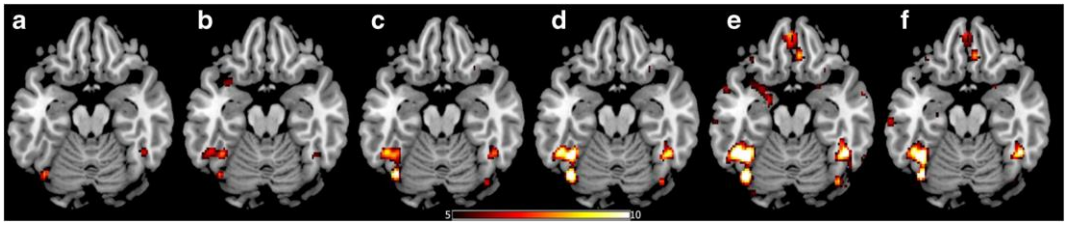

Fig. 17. Whole brain contrast maps from Volunteer 15, MB6. Bilateral fusiform face areas are identified based on ~11 min scanning with conventional EPI sequence (a.). The areas show up using multiband sequences with acceleration factor 6 and different scanning durations: 1/5FL (b.), 2/5FL (c.), 3/5FL (d.) 4/5FL (e.) and full scan length (f.). Every t-maps are thresholded at the same score (t>5).

4.1.2. Results of the ROI analysis: task-irrelevant regions

We also analysed the sampling rate effects in ROIs (PCC, lMPF and rMPF) where no relevant stimulus related activations were expected during the fMRI sessions.

Neither significant differences in activation levels ($t_{max}<2.5$, $p_{min}>0.21$) nor significant differences in t-scores ($t_{max}<2.4$, $p_{min}>0.54$) between on MB1 and higher sampling rate (MB4 and MB6) scans could be found.

4.2. Results of physiological noise correction in pre-surgical fMRI

4.2.1. Whole brain activation results

Jaccard coefficients were more than 0.5 in five cases while lower Jaccard values were found in other patients, the mean ± standard deviation was 0.27 ± 0.16. We considered the number of significant ($p < 0.001$) and non-significant ($p > 0.001$) voxels. We found significant differences between the original and physiological corrected activation maps in both cases ($p = 0.009$ and $p < 0.001$). Table 2 and Table 3 contains the Jaccard coefficients, the number of non-significant and significant voxels, the mean heart rate, the maximum amplitude of respiration and the detailed results of ROI analysis in all patients.

We detected moderately strong, significant positive correlation between the Jaccard index and heart rate ($R^2 = 0.31$, $p = 0.002$). However, we did not find significant correlations between the Jaccard index and respiration ($R^2 = 0.0052$, $p = 0.711$).

4.2.2. Results of ROI analysis

The ROIs' mean t-values were decreased after the physiological correction in every patient. We found significant differences ($p < 0.0015$) between the non-corrected and corrected region of interests at 5% significance level. The ROIs' standard deviations were also decreased, albeit – using Levene-test –significant differences have not been detected ($F = 0.28$).

We analyzed the extension of eloquent brain area activations and found significant differences between the uncorrected and physiological corrected maps ($p = 0.012$). Physiological correction decreased the extent of activations in all patients.

Table 2. The patients' sex (M: Male, F: Female), age, location of lesion, applied fMRI paradigms, variables of the non-corrected and physiological corrected fMRI activation maps

Patient ID	Applied paradigm; Coordinate of the maximum t-value	Jaccard Index	Number of significant (p<0.001) voxels – uncorrected map	Number of significant (p<0.001) voxels – corrected map	Number of non-significant (p>0.001) voxels – uncorrected map	Number of non-significant (p>0.001) voxels – corrected map
1.	Picture Naming [-42; 8; 37]	0.22	468	187	37151	37432
	Synonym [-40; 24; 35]	0.22	1943	946	35803	36800
2.	Picture Naming [-40; 21; 7]	0.27	2989	1241	42676	44424
	Synonym [41; 33; 14]	0.27	191	555	45518	45154
3.	Picture Naming [37; 18; 25]	0.22	2781	2297	35770	40610
4.	Picture Naming [-48; 8; 29]	0.24	3357	903	38242	40696
	Synonym [-32; 20; 29]	0.24	2502	1060	39157	40602
5.	Auditory Decision [-55; -47; 2]	0.59	1139	1239	48417	48317
	Picture Naming [-37; -55; -20]	0.17	583	336	48725	48972
	Synonym [-55; -47; 2]	0.56	1322	1663	48113	47772

Patient ID	Applied paradigm; Coordinate of the maximum t-value	Jaccard Index	Number of significant (p<0.001) voxels – uncorrected map	Number of significant (p<0.001) voxels – corrected map	Number of non-significant (p>0.001) voxels – uncorrected map	Number of non-significant (p>0.001) voxels – corrected map
6.	Finger tapping [-44; 26; 67]	0.17	415	344	39564	39635
	Picture Naming [-46; 6; 33]	0.36	4368	4055	35915	36228
	Synonym [-42; 24; 33]	0.12	366	423	39356	39299
7.	Finger tapping [42; -30; 49]	0.18	385	561	46443	46267
	Synonym [49; -33; 9]	0.28	1710	916	46334	47128
8.	Auditory Decision [-54; 14; 2]	0.54	1963	1822	45330	45471
	Picture Naming [-29; 38; 5]	0.67	6913	7175	40493	40231
	Synonym [-29; 37; 9]	0.39	3190	2220	44070	45040
9.	Finger tapping [39; -15; 60]	0.03	119	79	46605	46645
10.	Picture Naming [-55; 24; 11]	0.52	2304	1798	46577	47083
	Synonym [-37; 14; 17]	0.19	920	706	48071	48285

Patient ID	Applied paradigm; Coordinate of the maximum t-value	Jaccard Index	Number of significant (p<0.001) voxels – uncorrected map	Number of significant (p<0.001) voxels – corrected map	Number of non-significant (p>0.001) voxels – uncorrected map	Number of non-significant (p>0.001) voxels – corrected map
11.	Finger tapping [-39; 2; 55]	0.17	1069	882	46292	46479
	Picture Naming [-46; 7; 52]	0.12	625	482	46250	46393
	Synonym [-41; 20; 41]	0.11	302	252	46808	46858
12.	Picture Naming [-29; -6; 35]	0.15	532	265	43652	43919
	Synonym [-50; -7; 16]	0.18	640	276	43347	43711
13.	Auditory Decision [-35; 16; 34]	0.25	720	650	40002	40072
14.	Synonym [-27; 41; 25]	0.11	1579	1679	44725	44625
	Picture Naming [-50; 14; 28]	0.31	282	718	45834	45398

Table 3. The patients' sex (M: Male, F: Female), age, location of lesion, applied fMRI paradigms, variables of the non-corrected and physiological corrected fMRI activation maps and the detailed results of Region of interest analysis.

Patient ID	**Patient's age and sex**	**Name and localization of the lesion**	**Applied paradigm; Coordinate of the maximum t-value**	**Mean heartbeat [beats/min]**	**Maximum amplitude of respiration [arbitrary unit]**	**ROI without correction (mean ± std) [t-value]**	**ROI after correction (mean ± std) [t-value]**	**Jaccard Index**
1.	**62; F**	Left sided frontal glioma	Picture Naming [-42; 8; 37]	81	198	3.14 + 0.9	3.01 + 0.85	0.22
			Synonym [-40; 24; 35]	81	123	5.52 + 2.22	3.75 + 1.3	0.22
2.	**45; N**	Left sided, small frontal haemangioma	Picture Naming [-40; 21; 7]	81	124	2.65 + 1.19	2.51 + 0.91	0.27
			Synonym [41; 33; 14]	80	131	2.43 + 0.91	2.41 + 0.74	0.27
3.	**29; N**	Left sided, large fronto-temporal lesion	Picture Naming [37; 18; 25]	76	230	6.34 + 1.77	4.82 + 1.41	0.22
4.	**32; F**	Left sided temporal low-grade glioma	Picture Naming [-48; 8; 29]	82	346	3.2 + 0.89	2.65 + 0.65	0.24
			Synonym [-32; 20; 29]	81	282	3.05 + 1.32	2.98 + 1.12	0.24

Patient ID	Patient's age and sex	Name and localization of the lesion	Applied paradigm; Coordinate of the maximum t-value	Mean heartbeat [beats/min]	Maximum amplitude of respiration [arbitrary unit]	ROI without correction (mean ± std) [t-value]	ROI after correction (mean ± std) [t-value]	Jaccard Index
5.	**59; N**	Left sided temporo-occipital low-grade glioma	Auditory decision [-55; -47; 2]	68	271	4.65 + 2.19	4.61 + 2.2	0.59
			Picture Naming [-37; -55; -20]	69	220	3.11 + 1.63	2.85 + 1.38	0.17
			Synonym [-55; -47; 2]	72	291	3.67 + 1.89	3.36 + 1.01	0.56
6.	**39; N**	Left sided central glioma	Finger tapping [-44; 26; 67]	80	203			0.17
			Picture Naming [-46; 6; 33]	86	139	5.33 + 2.23	4.25 + 1.89	0.36
			Synonym [-42; 24; 33]	81	133	3,04 + 1.29	2.53 + 1.1	0.12
7.	**47; F**	Right sided, large glioblastoma multiforme	Finger tapping [42; -30; 49]	80	203	5.58 + 1.19	5.2 + 0.52	0.18
			Synonym [49; -33; 9]	81	177			0.28
8.	**51; F**	Left sided, fronto-temporal glioma	Auditory decision [-54; 14; 2]	77	101	5.35 + 2.45	4.97 + 2.13	0.54
			Picture Naming [-29; 38; 5]	75	131	5.95 + 2.98	5.76 + 1.91	0.67
			Synonym [-29; 37; 9]	77	125	3 + 2.52	2.55 + 1.78	0.39

Patient ID	Patient's age and sex	Name and localization of the lesion	Applied paradigm; Coordinate of the maximum t-value	Mean heartbeat [beats/min]	Maximum amplitude of respiration [arbitrary unit]	ROI without correction (mean ± std) [t-value]	ROI after correction (mean ± std) [t-value]	Jaccard Index
9.	**45; F**	Right sided, fronto-temporal low-grade glioma	Finger tapping [39; -15; 60]	98	212	4.11 + 0.91	3.9 + 0.55	0.03
10.	**50; F**	Left sided, central glioma	Picture Naming [-55; 24; 11]	81	607	3.11 + 0.94	3.01 + 0.66	0.52
			Synonym [-37; 14; 17]	80	498	3.65 + 1.21	3.01 + 0.96	0.19
11.	**47; F**	Left sided, central glioma	Finger tapping [-39; 2; 55]	80	203	3.14 + 0.62	2.69 + 1.11	0.17
			Picture Naming [-46; 7; 52]	81	298	2.34 + 1.16	1.84 + 0.72	0.12
			Synonym [-41; 20; 41]	81	223	2.51 + 1.04	3.17 + 0.99	0.11
12.	**52; N**	Left sided, large, fronto-temporal glioma	Picture Naming [-29; -6; 35]	85	139	2.93 + 1.18	2.87 + 1.15	0.15
			Synonym [-50; -7; 16]	87	227	5.66 + 1.09	5.65 + 1	0.18

Patient ID	Patient's age and sex	Name and localization of the lesion	Applied paradigm; Coordinate of the maximum t-value	Mean heartbeat [beats/min]	Maximum amplitude of respiration [arbitrary unit]	ROI without correction (mean ± std) [t-value]	ROI after correction (mean ± std) [t-value]	Jaccard Index
13.	**40; F**	Left sided, large temporo-parietal low-grade glioma	Auditory decision [-35; 16; 34]	84	220	4.87 + 1.01	4.54 + 0.88	0.25
14.	**44; N**	Left sided, fronto-temporal glioma	Synonym [-27; 41; 25]	86	229	2.1 + 0.89	2.1 + 0.88	0.11
			Picture Naming [-50; 14; 28]	86	139	2.32 + 0.59	2.11 + 0.77	0.31

We demonstrate the role of physiological noise correction in a pre-surgical setting in two cases.

In the first case (Fig 18.; Patient ID: 8; Picture Naming paradigm) a left sided, fronto-temporal glioma was detected with large extension into Broca's area. fMRI examination was performed for mapping the language areas, fMRI activation have larger extent (near the tumour) in the uncorrected map (red) compared with the physiological corrected activation map (blue). Only small changes were detected (white arrow) in the extent of the activations. Jaccard index was 0.67. With ROI analysis the mean and standard deviation of the t-values in the selected ROI was 5.95 ± 2.98 without and 5.76 ± 1.91 with correction (Table 2. contains the detailed results).

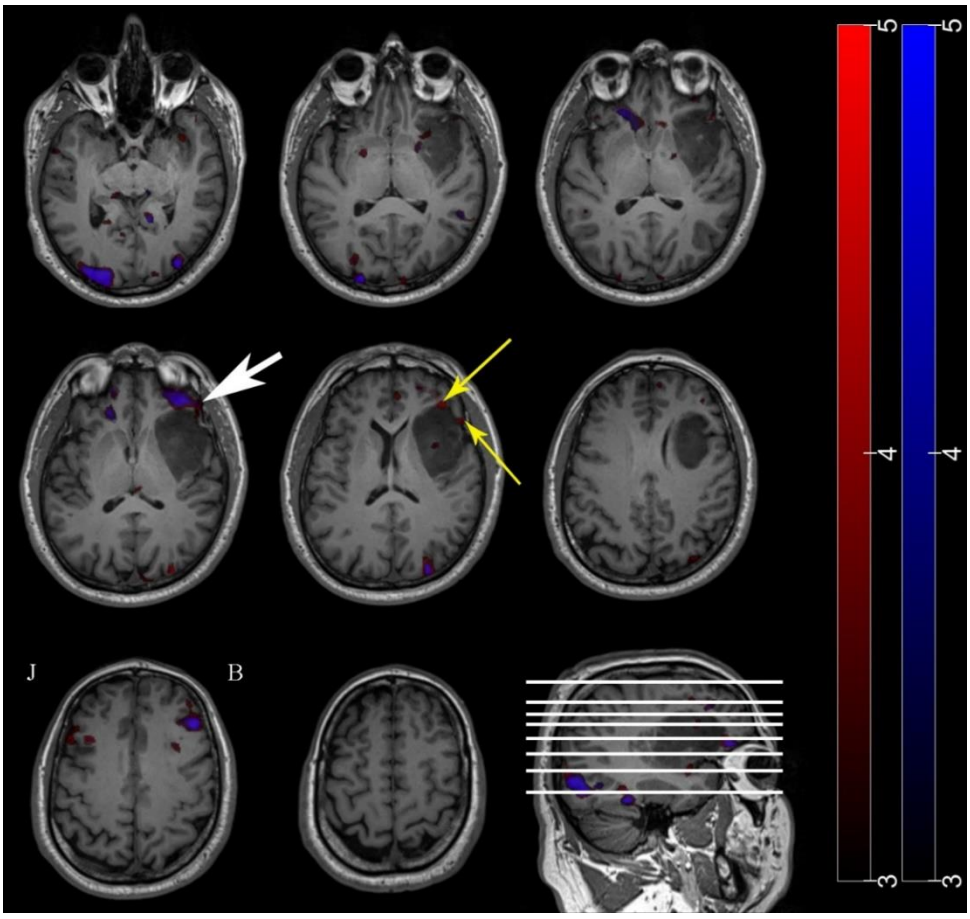

Fig 18. Left sided glioma was detected in Broca's area. The original, non-corrected (red) and the physiological corrected (blue) activation maps (t-values) show minimal differences according to the eloquent area (white arrow). Activations inside the tumour (yellow arrows) are disappeared after the physiological correction. L: left side, R: right side.

In the second case, a left sided glioma was detected near the Wernicke's area (Fig 19.; Patient ID: 5; Synonym paradigm). fMRI examination was performed to depict the language areas. A small fMRI activation was detected (white arrow) on the lateral side of the tumour, near the eloquent area. This activation was only visible on the original, non-corrected activation map, but disappeared if physiological correction had been performed (blue). On the same token, the extent of activation in Broca's area was larger on the uncorrected fMRI maps. There were activations deemed non-relevant (these were not related to the eloquent areas) in the axial slices (yellow arrows), however these activations were only visible on the uncorrected maps. The ROI analysis yielded mean and SD t-values of 3.67 ± 1.89 without correction and 3.36 ± 1.01 after correction (See Table 2. for details).

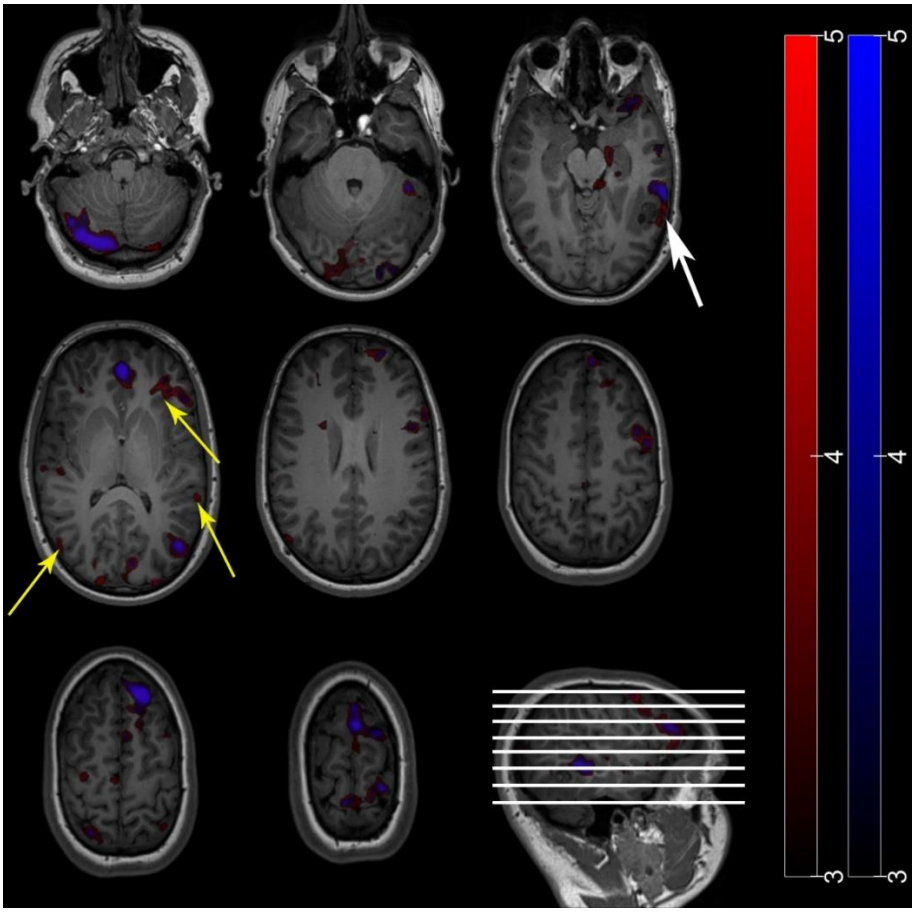

Fig 19. Left sided glioma was detected in Wernicke's region. The original, non-corrected (red) and the physiological corrected (blue) activation maps (t-values) show differences on the lateral side of the tumour (white arrow). Non-relevant activations depicted only the original, fMRI maps. L: left side, R: right side.

5. Discussion

5.1. Comparison of simultaneous multislice imaging and conventional EPI sequence

Our results showed that the multiband acquisition technique helps reducing the overall scanning time while maintains or improves the robustness of functional area localization at the single subject level. This could be very helpful in clinical practice. Indeed, by selecting appropriate acceleration factors the increase in temporal resolution counteracts the degradation of SNR caused by the change in "g-geometry factor" and T1 relaxation effects (Kawin Setsompop et al. 2012).

The SMS-CAIPIRINHA method with EPI was first demonstrated by Nunes et al. (Nunes et al. 2006). The necessary slice shifts were produced with a train of unipolar gradient blips on the slice axis. These blips introduced the desired phase difference between k-space lines effectively shifting overlapping slices in image-space. The main limitation of this early approach was the presence of concurrent effective dephasing across the slices. Setsompop et al. solved this problem with applying blipped rewinder gradients to keep phase accumulation within a dedicated range, thus maintaining the relative phase-differences while decreasing the through-slice dephasing. This blipped CAIPIRINHA acquisition method indeed decreases the noise amplification in SMS EPI measurements (Lutti et al. 2013). However, imperfect slice separation could still result in residual aliasing along slices referred as "slice leakage" in the literature (Kawin Setsompop et al. 2012). There are different strategies to circumvent this issue at the reconstruction level, from which we chose the leak-block kernel reconstruction approach. This method suppresses the prevalence of slice-leakage artefacts significantly at the price of mild SNR decrease. Hence, the probability of false-positive activation is kept low (Todd et al. 2016). More sampling points mean better temporal resolution with increased degrees-of-freedom. This allows the application of multiband sequences as an advanced strategy for independent component analysis at resting-state fMRI.

In order to quantify the efficiency of multiband sequences and define the necessary measurement duration for fMRI localizer examinations, truncated SMS

scans (with MB acceleration factors 4 and 6) were compared with a conventional, full-scan length (~11 min longs) EPI sequence.

The application of a rapid event related fMRI design not only enabled us to collect data with enough evoked responses within less than 3 minutes in our truncated segments, but also made data whitening (removal of a fitted AR model) less vital in the preprocessing pipeline as temporal autocorrelation is less likely to serve as a confound during a relatively high frequency stimulus presentation with proper temporal jittering (Sahib et al. 2016).

To test brain areas with different magnetic susceptibility and SNR characteristics (Keil et al. 2013) we chose our ROIs (FFA, PPA and EBA) to be at different depth in the brain. While FFA has a small activated volume, it can be found close to areas with high magnetic susceptibility, whereas PPA, with its deep location, is expected to have lower SNR characteristics.

5.1.1. Impact of higher temporal resolution and reduced scan time on t-scores

We found in agreement with the pertinent literature (L. Chen et al. 2015; Lutti et al. 2013) that SMS sequences with MB acceleration factors up to 6 (approximately 2.5Hz temporal resolution) would increase the sensitivity of the task-based, event related fMRI analyses, when comparing acquisitions with equal scanning length (we compared the MB1 measurement – with full scan length – with MB measurements using 4 and 6 acceleration factor).

5.1.2. Comparison of sampling rate at 1Hz with reduced scanning time vs 0.5Hz (MB4 vs MB1)

As a general conclusion, 40% of the full scan time (2/5FL) with acceleration factor of 4 (1Hz sampling rate) is enough to reach similar t-scores than with conventional EPI sequences (0.5Hz sampling rate (MB1)), without acceleration – see Figure 13-15. In the PPA ROI significantly higher statistical values are achieved, using at least 60% (3/5FL) of the scan time compare with the conventional MB1 acquisition technique with 11 min long scan (FL). The 4/5FL

scanning measurements with acceleration factor of 4 outperform the MB1 based scans in two of the localized functional areas (PPA, EBA).

5.1.3. Comparison of sampling rate at ~2.5Hz with reduced scanning time vs. 0.5Hz (MB6 vs MB1)

Shorter scan time with acceleration factor 6 reached similar or better results (t-scores) than the MB1 full scan-length sessions (Fig 13.,14.,15. b.) in almost all cases (except the EBA ROI). It means that in most cases approximately 2 min scanning (1/5FL) at ~2.5Hz sampling rate (MB6) provides similar or better localization sensitivity than the 11 min FL session at 0.5Hz sampling rate. Moreover, an MB6 acquisition provides significantly higher t-scores in all functional areas already with 8 min scanning (4/5FL) time. Regarding the FFA ROI even 2/5FL (4 min) long measurements yielded significantly higher t-scores compared to FL MB1 (Fig 14. b.).

5.1.4. Specificity, effect of temporal autocorrelation

As Sahib et al. showed (Sahib et al. 2016), major improvement of temporal resolution also increases temporal autocorrelation – with the risk to influence statistical significance and by increasing the rate of false positive results during fMRI analysis. In order to avoid complex and equivocal estimation of the effect of noise we also examined sampling rate effects in other brain regions where no significant activation was expected for our tasks. We have chosen two ROIs (PCC and bilateral MPF) from the default mode network because several studies showed high amplitude background activity in these regions during task-based paradigms (Koshino et al. 2015; DeSalvo et al. 2014), that may pose as a major source for false positives.

We did not find significant activations in the above mentioned DMN ROIs, so our results show that the investigated multiband acquisition technique did not impair the specificity of t-fMRI regardless the acceleration factor chosen. Indeed, we found neither significant activations nor significant differences between the statistical scores based on MB1 and higher sampling rate (MB4 and MB6) acquisitions at group-level in the DMN ROIs.

5.1.5. Demonstration of higher temporal resolution at the subject level

We also wanted to investigate if multiband sequences can be used efficiently in the clinical practice, thus we have analysed the results of higher sampling rate measurements at the single subject level based on a representative sample around the FFA region. Our general conclusion was that peak t-scores were higher and spatial extent of FFA activations were larger when using 1Hz or ~2.5Hz sampling rate compared to 0.5 Hz. Note, that there were several subjects whose activation statistics did not follow a clear positive trend with higher temporal resolution in case of very short scanning duration (e.g. 1/5FL, 2/5L or 3/5FL yielded lower t-scores compared to FL with MB1). Statistical maps obtained with 8 min scan duration (4/5FL) were either indistinguishable or showed even more robust activations than the ones obtained with full length scanning without acceleration (MB1).

Our results indicate that the application of multiband sequences can significantly reduce the required scan time for localization purposes while retaining (or even improving on) the sensitivity and specificity of the traditional fMRI scanning sequences.

5.2. Physiological noise correction for pre-surgical fMRI

In this study we examined the role of model-based physiological noise correction in presurgical, task-based functional MRI. We concentrated on the eloquent language areas (Broca and Wernicke).

Most of the research groups use simple temporal filtering to eliminate physiological noise, as part of the standard data analysis pipeline. Nevertheless, several studies revealed (e.g. Tong and Frederick (‘Frontiers | Studying the Spatial Distribution of Physiological Effects on BOLD Signals Using Ultrafast FMRI |

Frontiers in Human Neuroscience' n.d.)), that getting rid of the physiological noise components via this formula is almost impossible, due to the long repetition time leading to under-sampling and aliasing of physiological signals. Indeed, temporal filtering would only work with shorter repetition times (<400 ms). In consequence, there are several methods/toolboxes available that provide more sophisticated physiological noise correction in order limit the proportion of false positive activation.

Many studies confirmed, that physiological noise can spoil the results of functional MRI analysis, especially in case of resting-state, which is based upon the low-frequency fluctuations of the fMRI signal. Catie Chang and Gary H. Glover showed the impact of model-based RETROICOR for resting-state fMRI, concentrating on the Default Mode Network's correlations and anti-correlations (Chang and Glover 2009). They also drew our attention to the importance of cardiac response function in rs-fMRI (Chang, Cunningham, and Glover 2009). Ludovica Griffanti et al. worked with a data-driven, ICA-based correction technique (FIX) (Griffanti et al. 2014). They used MB accelerated acquisition and applied single-subject independent component analysis, followed by automatic component classification with FMRIB's ICA-based X_noiseifier (FIX) to identify and remove the apparent artefacts. They showed the physiological noise related independent components follow arteries and veins (e.g. the anterior, middle and posterior cerebral arteries). They also highlighted that independent component analysis is very helpful to determine spatial and temporal characteristics of the physiological noise related artefacts and separate them from "real" BOLD fluctuation signals.

Nevertheless only a few studies have used physiological correction for task-based fMRI (Hutton et al. 2011; Hillenbrand, Ivry, and Schlerf 2016; Sahib et al. 2018).

In our study we determined the effects of cardiac and respiratory function on the activation maps in a presurgical, task-based functional MRI setting. We investigated whether we can reduce false positive activations with physiological noise correction. We hypothesized that more precise activation maps will be available with physiological noise correction, that are better suited for the presurgical planning.

5.2.1. Physiological noise correction at whole brain fMRI

We demonstrated, that physiological artefact correction modifies the whole brain activation maps in presurgical, task-based functional MRI. Jaccard indexes were – except for 5 cases – low (<0.5) so we concluded that the uncorrected and corrected statistical maps were substantially different. In order to better understand the above-mentioned differences and to determine how the model-based RETORICOR/RVHR modifies the statistical maps, we also analysed the number of significant ($p < 0.001$) voxels and the number of non-significant ($p > 0.001$) voxels. Physiological correction reduced the number of significant voxels in 23 cases, leading to a significant difference ($p < 0.009$) between the corrected and non-corrected maps on the group level. Furthermore, upon physiological noise correction there was a decrease of activations in irrelevant brain areas, not related to the actual paradigms ($p < 0.001$).

5.2.2. Physiological noise correction at ROI analysis

Physiological correction provided more precise functional MRI activations at the eloquent brain areas. We found significant differences ($p < 0.05$) between the ROIs' mean values. After physiological correction the activations at the eloquent areas remained significant at $p < 0.001$ significant level. We also found decreased standard deviation values in the ROIs, but this reduction was not significant. However – with the decreased standard deviation – we can conclude, that more reliable activation maps are available after the physiological correction.

We examined the extent of the relevant/eloquent clusters/activations and found significant ($p = 0.012$) differences between corrected and uncorrected maps, with corrected maps showing less extensive activations. These findings corroborate the relevance of physiological noise correction.

5.3. Simultaneous multislice imaging at task-based functional MRI - Conclusion

One of the major problems in clinical – and also in some research oriented – functional MRI is long scanning time. In this study, we analysed the beneficial effects of the simultaneous multislice based acceleration technique quantitatively. We examined the performance of the standard fMRI analysis method in relation to three different sampling frequencies in three target ROIs: EBA, FFA, PPA. We showed that the same statistical power can be reached using SMS sequences (increasing temporal resolution) even with serious scan time reduction using appropriate MB sequences with proper acceleration. Based on our experiments an 11 min long classical (unaccelerated) localizer scan can be replaced safely with a 4 min accelerated acquisition with multiband factor 6 using ~2.5Hz sampling rate. It could be very helpful, especially when patient cooperation is a real problem even within this relatively short time-frame. With accelerated scans very similar statistical results can be reached compared to those of a standard-length protocol – without acceleration.

So far, the usage of the MB sequences in the clinical routine is still not widespread despite the many advantages of the accelerated acquisitions. This may be due to the relative novelty of the technique and the challenges posed by the different implementations across vendors. Note, that there are several vendors, who provide original, built-in SMS sequences without any manual installation/intervention. It is worth noting that false-positive activations could appear in case of one slice leaking into other simultaneously exited slices when using MB sequences, albeit these artefactual activations can be controlled with new reconstruction techniques e.g. blipped-CAIPI.

In this study we used a special paradigm based on complex visual stimuli to demonstrate the efficiency of higher temporal resolution (with lower scan time) obtained with difference acceleration factors at higher order visual areas, namely EBA, FFA and PPA. Importantly SMS sequences can be used not only for research studies with complex cognitive paradigms and questions, but clinical practice can also benefit from introducing SMS based acceleration in the daily routine, especially cases where patient cooperation is restricted.

5.4. Retrospective physiological noise correction at presurgical task-based functional MRI - Conclusion

In this study we demonstrated the efficiency of model-based physiological correction technique, which works in the image space and uses the hear-rate and cardiac variability to reduce the physiological based artefacts. We analysed the effect of physiological noises in a special case, namely presurgical task-based fMRI.

RETROICOR/RVHR reduced the false-positive results and provided more reliable statistical maps. Although ROI analysis revealed that the calculated activation amplitudes decreased after physiological correction, the spatial specificity of the eloquent brain activations increased. These findings need further validation using other modalities, like invasive electrocorticography.

The primary concern in presurgical fMRI is having false negative results. In principle, applying this retrospective, model-based correction technique the statistical activation threshold can be lowered – increasing the sensitivity of the analysis – without introducing excessive false positive activations.

We can conclude, that RETROICOR/RVHR can reduce the physiological artefacts. Physiological correction can significantly improve fMRI activation maps, while reducing the false positive results. This in turn leads to more reliable statistical maps and helps to characterizing eloquent brain activations and improving the efficiency of presurgical planning.

6. Summary

Two-dimensional simultaneous multi-slice echo planar imaging is a relatively new special Magnetic Resonance Imaging sequence for accelerating the acquisition. This faster acquisition can be used to record more volumes and it is well suited for improving the sensitivity of task-based and resting-state fMRI imaging.

Physiological noise may seriously influence the fMRI analysis. The effect of physiological noise is well known, and several toolboxes are available to reduce the physiological based artefacts. These techniques may help to improve the sensitivity and specificity of task- and resting-state functional MRI.

In this thesis I examined the relevance of simultaneous multi-slice (SMS) EPI sequence at task-based functional MRI. I compared the conventional, full scan length EPI measurements with SMS sequences with acceleration factor of four and six. In the second part of my thesis I used RETROICOR/RVHR toolbox to reveal the role of physiological noise correction at per-surgical functional MRI.

SMS sequences with MB acceleration factors up to 6 (approximately 2.5Hz temporal resolution) would increase the sensitivity of the task-based, event related fMRI analysis. Based on my experiments a conventional, 11 min long (unaccelerated) EPI scan can be safely replaced with a 4 min accelerated acquisition with multiband factor 6 using ~2.5Hz sampling rate. It could be very helpful, especially when patient cooperation is a real problem and shorter acquisition is necessary.

Physiological correction provided more precise functional MRI activations at the eloquent brain areas. RETROICOR/RVHR reduced the false-positive results and provided more reliable statistical maps. Nevertheless, ROI analysis revealed that the calculated activation amplitudes decreased after physiological correction. The spatial specificity of the eloquent brain activations increased.

7. Összefoglalás

A *simultaneous multi-slice* (SMS) vagy más néven *multiband* (MB) egy echo planar imaging (EPI) alapú, mágneses rezonanciás (MR) szekvencia, amely relatíve új mérési eljárás. Alkalmazásával gyorsabb akvizícióra van lehetőség, így a mérési idő jelentősen csökkenthető. Ezzel párhuzamosan javítható mind a feladathoz kötött-, mind a nyugalmi állapotú funkcionális MRI (fMRI) vizsgálatok szenzitivitása.

A fiziológiai jellegű (légzési és keringési eredetű) műtermékek jelentősen befolyásolhatja az fMRI adatelemzést. Az ilyen típusú műtermékek csökkentésére számos algoritmus/szoftver alkalmazható, így jelentős mértékben javítható a feladathoz kötött- és nyugalmi állapotú fMRI vizsgálatok szenzitivitása és specificitása.

A tézis első felében az SMS EPI szekvenciák jelentőségét vizsgáltam feladathoz kötött fMRI vizsgálatoknál. Összehasonlítottam a konvencionális, teljes hosszúságú, gyorsítás nélküli szekvenciát a különböző gyorsítási faktorú SMS szekvenciákkal. A tézisem második részében arra kerestem a választ, hogy a fiziológiai műtermékeknek milyen jelentősége van a műtéti tervezéshez használt, feladathoz kötött fMRI vizsgálatoknál. Az elemzéshez RETROICOR/RVHR toolboxot használtam.

Az SMS szekvenciák (hatos gyorsítási faktorral; ~2.5Hz-es időbeli felbontás) javították a feladathoz kötött fMRI vizsgálatok szenzitivitását. Vizsgálatom alapján megállapítható, hogy a hagyományos, 11 perc hosszúságú, gyorsítás nélküli EPI szekvencia biztonságosan kiváltható egy 4 perces, hatos gyorsítási faktorú SMS szekvenciával. Ez nagyon fontos lehet, olyan esetekben, amikor a beteggel való kooperáció nehezített.

A fiziológiai műtermékek korrekciójával a kapott fMRI-s aktivációs mintázat megbízhatóbbá válik. A RETROICOR/RVHR használatával csökkenthetők a fals pozitív eredmények, mindazonáltal az elvégzett ROI-s elemzés alapján megállapítható, hogy fiziológiai korrekció után az aktivációk erőssége/amplitúdója csökken. Az elokvens területekre vonatkozó aktivációk térbeli specificitása viszont javul.

8. References

American Society of Functional Neuroradiology. 2007. ‘FMRI BOLD Paradigms’. https://www.asfnr.org/paradigms/.

Bandettini, P. A., E. C. Wong, R. S. Hinks, R. S. Tikofsky, and J. S. Hyde. 1992. ‘Time Course EPI of Human Brain Function during Task Activation’. *Magnetic Resonance in Medicine* 25 (2): 390–97.

Barth, Markus, Felix Breuer, Peter J. Koopmans, David G. Norris, and Benedikt A. Poser. 2016. ‘Simultaneous Multislice (SMS) Imaging Techniques’. *Magnetic Resonance in Medicine* 75 (1): 63–81. https://doi.org/10.1002/mrm.25897.

Beckmann, Christian F. 2012. ‘Modelling with Independent Components’. *NeuroImage*, 20 YEARS OF fMRI, 62 (2): 891–901. https://doi.org/10.1016/j.neuroimage.2012.02.020.

Begg, Colin B. 1988. ‘Statistical Methods in Medical Research P. Armitage and G. Berry, Blackwell Scientific Publications, Oxford, U.K., 1987. No. of Pages: 559. Price £22.50’. *Statistics in Medicine* 7 (7): 817–18. https://doi.org/10.1002/sim.4780070711.

Behzadi, Yashar, Khaled Restom, Joy Liau, and Thomas T. Liu. 2007. ‘A Component Based Noise Correction Method (CompCor) for BOLD and Perfusion Based FMRI’. *NeuroImage* 37 (1): 90–101. https://doi.org/10.1016/j.neuroimage.2007.04.042.

Birn, R. M., P. A. Bandettini, R. W. Cox, and R. Shaker. 1999. ‘Event-Related FMRI of Tasks Involving Brief Motion’. *Human Brain Mapping* 7 (2): 106–14.

Birn, Rasmus M. 2012. ‘The Role of Physiological Noise in Resting-State Functional Connectivity’. *NeuroImage*, 20 YEARS OF fMRI, 62 (2): 864–70. https://doi.org/10.1016/j.neuroimage.2012.01.016.

Birn, Rasmus M., Maria Daniela Cornejo, Erin K. Molloy, Rémi Patriat, Timothy B. Meier, Gregory R. Kirk, Veena A. Nair, M. Elizabeth Meyerand, and Vivek Prabhakaran. 2014. ‘The Influence of Physiological Noise Correction on Test–Retest Reliability of Resting-State Functional Connectivity’. *Brain Connectivity* 4 (7): 511–22. https://doi.org/10.1089/brain.2014.0284.

Birn, Rasmus M., Jason B. Diamond, Monica A. Smith, and Peter A. Bandettini. 2006. ‘Separating Respiratory-Variation-Related Fluctuations from Neuronal-Activity-

Related Fluctuations in FMRI'. *NeuroImage* 31 (4): 1536–48. https://doi.org/10.1016/j.neuroimage.2006.02.048.

Birn, Rasmus M., Monica A. Smith, Tyler B. Jones, and Peter A. Bandettini. 2008. 'The Respiration Response Function: The Temporal Dynamics of FMRI Signal Fluctuations Related to Changes in Respiration'. *NeuroImage* 40 (2): 644–54. https://doi.org/10.1016/j.neuroimage.2007.11.059.

Bloch, F., W. W. Hansen, and M. Packard. 1946. 'The Nuclear Induction Experiment'. *Physical Review* 70 (7–8): 474–85. https://doi.org/10.1103/PhysRev.70.474.

Brainard, DH. 1997. 'The Psychophysics Toolbox'. *Spat Vis.* 10 (4): 433–36.

Breuer, Felix A., Martin Blaimer, Robin M. Heidemann, Matthias F. Mueller, Mark A. Griswold, and Peter M. Jakob. 2005. 'Controlled Aliasing in Parallel Imaging Results in Higher Acceleration (CAIPIRINHA) for Multi-Slice Imaging'. *Magnetic Resonance in Medicine* 53 (3): 684–91. https://doi.org/10.1002/mrm.20401.

Buxton, R. B., and L. R. Frank. 1997. 'A Model for the Coupling between Cerebral Blood Flow and Oxygen Metabolism during Neural Stimulation'. *Journal of Cerebral Blood Flow and Metabolism: Official Journal of the International Society of Cerebral Blood Flow and Metabolism* 17 (1): 64–72. https://doi.org/10.1097/00004647-199701000-00009.

Buxton, R. B., E. C. Wong, and L. R. Frank. 1998. 'Dynamics of Blood Flow and Oxygenation Changes during Brain Activation: The Balloon Model'. *Magnetic Resonance in Medicine* 39 (6): 855–64.

Cauley, Stephen F., Jonathan R. Polimeni, Himanshu Bhat, Lawrence L. Wald, and Kawin Setsompop. 2014. 'Interslice Leakage Artifact Reduction Technique for Simultaneous Multislice Acquisitions: Interslice Leakage Artifact Reduction Technique'. *Magnetic Resonance in Medicine* 72 (1): 93–102. https://doi.org/10.1002/mrm.24898.

Chang, Catie, John P. Cunningham, and Gary H. Glover. 2009. 'Influence of Heart Rate on the BOLD Signal: The Cardiac Response Function'. *NeuroImage* 44 (3): 857–69. https://doi.org/10.1016/j.neuroimage.2008.09.029.

Chang, Catie, and Gary H. Glover. 2009. ‘Effects of Model-Based Physiological Noise Correction on Default Mode Network Anti-Correlations and Correlations’. *NeuroImage* 47 (4): 1448–59. https://doi.org/10.1016/j.neuroimage.2009.05.012.

Chapman, B., R. Turner, R. J. Ordidge, M. Doyle, M. Cawley, R. Coxon, P. Glover, and P. Mansfield. 1987. ‘Real-Time Movie Imaging from a Single Cardiac Cycle by NMR’. *Magnetic Resonance in Medicine* 5 (3): 246–54.

Chen, Jingyuan E., and Gary H. Glover. 2015. ‘Functional Magnetic Resonance Imaging Methods’. *Neuropsychology Review* 25 (3): 289–313. https://doi.org/10.1007/s11065-015-9294-9.

Chen, L., A. T. Vu, J. Xu, S. Moeller, K. Ugurbil, E. Yacoub, and D.A. Feinberg. 2015. ‘Evaluation of Highly Accelerated Simultaneous Multi-Slice EPI for FMRI’. *NeuroImage* 104 (January): 452–59. https://doi.org/10.1016/j.neuroimage.2014.10.027.

Dagli, M. S., J. E. Ingeholm, and J. V. Haxby. 1999. ‘Localization of Cardiac-Induced Signal Change in FMRI’. *NeuroImage* 9 (4): 407–15. https://doi.org/10.1006/nimg.1998.0424.

Davis, T. L., K. K. Kwong, R. M. Weisskoff, and B. R. Rosen. 1998. ‘Calibrated Functional MRI: Mapping the Dynamics of Oxidative Metabolism’. *Proceedings of the National Academy of Sciences of the United States of America* 95 (4): 1834–39.

DeSalvo, Matthew N., Linda Douw, Shigetoshi Takaya, Hesheng Liu, and Steven M. Stufflebeam. 2014. ‘Task-Dependent Reorganization of Functional Connectivity Networks during Visual Semantic Decision Making’. *Brain and Behavior* 4 (6): 877–85. https://doi.org/10.1002/brb3.286.

Deshmane, Anagha, Vikas Gulani, Mark A. Griswold, and Nicole Seiberlich. 2012. ‘Parallel MR Imaging’. *Journal of Magnetic Resonance Imaging : JMRI* 36 (1): 55–72. https://doi.org/10.1002/jmri.23639.

Diukova, Ana, Jennifer Ware, Jessica E. Smith, C. John Evans, Kevin Murphy, Peter J. Rogers, and Richard G. Wise. 2012. ‘Separating Neural and Vascular Effects of Caffeine Using Simultaneous EEG–FMRI: Differential Effects of Caffeine on Cognitive and Sensorimotor Brain Responses’. *Neuroimage* 62 (1): 239–49. https://doi.org/10.1016/j.neuroimage.2012.04.041.

Downing, P. E. 2001. ‘A Cortical Area Selective for Visual Processing of the Human Body’. *Science* 293 (5539): 2470–73. https://doi.org/10.1126/science.1063414.

Eichner, Cornelius, Kourosh Jafari-Khouzani, Stephen Cauley, Himanshu Bhat, Pavlina Polaskova, Ovidiu C. Andronesi, Otto Rapalino, et al. 2014. ‘Slice Accelerated Gradient-Echo Spin-Echo Dynamic Susceptibility Contrast Imaging with Blipped CAIPI for Increased Slice Coverage’. *Magnetic Resonance in Medicine* 72 (3): 770–78. https://doi.org/10.1002/mrm.24960.

Epstein, Russell, and Nancy Kanwisher. 1998. ‘A Cortical Representation of the Local Visual Enviroment.’ *Nature* 392 (6676): 598–601. https://doi.org/10.1038/33402.

Farràs-Permanyer, Laia, Joan Guàrdia-Olmos, and Maribel Peró-Cebollero. 2015. ‘Mild Cognitive Impairment and FMRI Studies of Brain Functional Connectivity: The State of the Art’. *Frontiers in Psychology* 6 (August). https://doi.org/10.3389/fpsyg.2015.01095.

Feinberg, David A., Steen Moeller, Stephen M. Smith, Edward Auerbach, Sudhir Ramanna, Matthias Gunther, Matt F. Glasser, Karla L. Miller, Kamil Ugurbil, and Essa Yacoub. 2010. ‘Multiplexed Echo Planar Imaging for Sub-Second Whole Brain FMRI and Fast Diffusion Imaging’. *PloS One* 5 (12): e15710. https://doi.org/10.1371/journal.pone.0015710.

Feinberg, David A., Timothy G. Reese, and Van J. Wedeen. 2002. ‘Simultaneous Echo Refocusing in EPI’. *Magnetic Resonance in Medicine* 48 (1): 1–5. https://doi.org/10.1002/mrm.10227.

Feinberg, David A., and Kawin Setsompop. 2013. ‘Ultra-Fast MRI of the Human Brain with Simultaneous Multi-Slice Imaging’. *Journal of Magnetic Resonance* 229 (April): 90–100. https://doi.org/10.1016/j.jmr.2013.02.002.

Fox, P T, and M E Raichle. 1986. ‘Focal Physiological Uncoupling of Cerebral Blood Flow and Oxidative Metabolism during Somatosensory Stimulation in Human Subjects.’ *Proceedings of the National Academy of Sciences of the United States of America* 83 (4): 1140–44.

Frank, L. R., R. B. Buxton, and E. C. Wong. 2001. ‘Estimation of Respiration-Induced Noise Fluctuations from Undersampled Multislice FMRI Data’. *Magnetic Resonance in Medicine* 45 (4): 635–44.

‘Frontiers | Studying the Spatial Distribution of Physiological Effects on BOLD Signals Using Ultrafast FMRI | Frontiers in Human Neuroscience’. n.d. Accessed 28 March 2019. https://www.frontiersin.org/articles/10.3389/fnhum.2014.00196/full.

‘Functional Connectivity in the Motor Cortex of Resting Human Brain Using Echo-planar Mri - Biswal - 1995 - Magnetic Resonance in Medicine - Wiley Online Library’. n.d. Accessed 29 March 2019. https://onlinelibrary.wiley.com/doi/abs/10.1002/mrm.1910340409#.

‘GIFT Software’. n.d. Accessed 1 April 2019. http://mialab.mrn.org/software/gift/index.html.

Glockner, James F., Houchun H. Hu, David W. Stanley, Lisa Angelos, and Kevin King. 2005. ‘Parallel MR Imaging: A User’s Guide’. *RadioGraphics* 25 (5): 1279–97. https://doi.org/10.1148/rg.255045202.

Glover, G. H., T. Q. Li, and D. Ress. 2000. ‘Image-Based Method for Retrospective Correction of Physiological Motion Effects in FMRI: RETROICOR’. *Magnetic Resonance in Medicine* 44 (1): 162–67.

Glover, Gary H. 2011. ‘Overview of Functional Magnetic Resonance Imaging’. *Neurosurgery Clinics of North America* 22 (2): 133–39. https://doi.org/10.1016/j.nec.2010.11.001.

Griffanti, Ludovica, Gwenaëlle Douaud, Janine Bijsterbosch, Stefania Evangelisti, Fidel Alfaro-Almagro, Matthew F. Glasser, Eugene P. Duff, et al. 2017. ‘Hand Classification of FMRI ICA Noise Components’. *NeuroImage*, Cleaning up the fMRI time series: Mitigating noise with advanced acquisition and correction strategies, 154 (July): 188–205. https://doi.org/10.1016/j.neuroimage.2016.12.036.

Griffanti, Ludovica, Gholamreza Salimi-Khorshidi, Christian F. Beckmann, Edward J. Auerbach, Gwenaëlle Douaud, Claire E. Sexton, Enikő Zsoldos, et al. 2014. ‘ICA-Based Artefact Removal and Accelerated FMRI Acquisition for Improved Resting State Network Imaging’. *NeuroImage* 95 (July): 232–47. https://doi.org/10.1016/j.neuroimage.2014.03.034.

Griswold, Mark A., Peter M. Jakob, Robin M. Heidemann, Mathias Nittka, Vladimir Jellus, Jianmin Wang, Berthold Kiefer, and Axel Haase. 2002. ‘Generalized

Autocalibrating Partially Parallel Acquisitions (GRAPPA)'. *Magnetic Resonance in Medicine* 47 (6): 1202–10. https://doi.org/10.1002/mrm.10171.

Grover, Vijay P.B., Joshua M. Tognarelli, Mary M.E. Crossey, I. Jane Cox, Simon D. Taylor-Robinson, and Mark J.W. McPhail. 2015. 'Magnetic Resonance Imaging: Principles and Techniques: Lessons for Clinicians'. *Journal of Clinical and Experimental Hepatology* 5 (3): 246–55. https://doi.org/10.1016/j.jceh.2015.08.001.

Handwerker, Daniel A., John M. Ollinger, and Mark D'Esposito. 2004. 'Variation of BOLD Hemodynamic Responses across Subjects and Brain Regions and Their Effects on Statistical Analyses'. *NeuroImage* 21 (4): 1639–51. https://doi.org/10.1016/j.neuroimage.2003.11.029.

Hegyi, Márta, Zsuzsa Siegler, Péter Barsi, Gábor Rudas, Zsolt Lengyel, Szabolcs Szakáll, László Bognar, Lajos Rudolf Kozak, Magdolna Neuwirth, and András Fogarasi. 2009. '[Surgical treatment of resistant epilepsy, caused by hemispherical dysgenesis--case report]'. *Ideggyogyaszati Szemle* 62 (5–6): 185–89.

Hermann, Petra, Mareike Grotheer, Gyula Kovács, and Zoltán Vidnyánszky. 2017. 'The Relationship between Repetition Suppression and Face Perception'. *Brain Imaging and Behavior* 11 (4): 1018–28. https://doi.org/10.1007/s11682-016-9575-9.

Hillenbrand, Sarah F., Richard B. Ivry, and John E. Schlerf. 2016. 'Impact of Task-Related Changes in Heart Rate on Estimation of Hemodynamic Response and Model Fit'. *NeuroImage* 132 (May): 455–68. https://doi.org/10.1016/j.neuroimage.2016.02.068.

'Home | MRIcroGL | University of South Carolina'. n.d. Accessed 9 January 2018. http://www.mccauslandcenter.sc.edu/mricrogl/home.

Hutton, C., O. Josephs, J. Stadler, E. Featherstone, A. Reid, O. Speck, J. Bernarding, and N. Weiskopf. 2011. 'The Impact of Physiological Noise Correction on FMRI at 7T'. *NeuroImage* 57 (1): 101–12. https://doi.org/10.1016/j.neuroimage.2011.04.018.

James, Jija S., Pg Rajesh, Anuvitha Vs Chandran, and Chandrasekharan Kesavadas. 2014. 'FMRI Paradigm Designing and Post-Processing Tools'. *The Indian*

Journal of Radiology & Imaging 24 (1): 13–21. https://doi.org/10.4103/0971-3026.130686.

Kahan, Joshua, Maren Urner, Rosalyn Moran, Guillaume Flandin, Andre Marreiros, Laura Mancini, Mark White, et al. 2014. 'Resting State Functional MRI in Parkinson's Disease: The Impact of Deep Brain Stimulation on "Effective" Connectivity'. *Brain* 137 (4): 1130–44. https://doi.org/10.1093/brain/awu027.

Kanwisher, N., J. McDermott, and M. M. Chun. 1997. 'The Fusiform Face Area: A Module in Human Extrastriate Cortex Specialized for Face Perception'. *The Journal of Neuroscience: The Official Journal of the Society for Neuroscience* 17 (11): 4302–11.

Kasper, Lars, Steffen Bollmann, Andreea O. Diaconescu, Chloe Hutton, Jakob Heinzle, Sandra Iglesias, Tobias U. Hauser, et al. 2017. 'The PhysIO Toolbox for Modeling Physiological Noise in FMRI Data'. *Journal of Neuroscience Methods* 276: 56–72. https://doi.org/10.1016/j.jneumeth.2016.10.019.

Keil, Boris, James N. Blau, Stephan Biber, Philipp Hoecht, Veneta Tountcheva, Kawin Setsompop, Christina Triantafyllou, and Lawrence L. Wald. 2013. 'A 64-Channel 3T Array Coil for Accelerated Brain MRI'. *Magnetic Resonance in Medicine* 70 (1): 248–58. https://doi.org/10.1002/mrm.24427.

Kesavadas, Chandrasekharan, and Bejoy Thomas. 2008. 'Clinical Applications of Functional MRI in Epilepsy'. *Indian Journal of Radiology and Imaging* 18 (3): 210. https://doi.org/10.4103/0971-3026.41829.

Koshino, Hideya, Takehiro Minamoto, Ken Yaoi, Mariko Osaka, and Naoyuki Osaka. 2015. 'Coactivation of the Default Mode Network Regions and Working Memory Network Regions during Task Preparation'. *Scientific Reports* 4 (1). https://doi.org/10.1038/srep05954.

Kozák, Lajos R., Szabolcs Dávid, Gábor Rudas, Zoltán Vidnyánszky, Alexander Leemans, and Zoltán Nagy. 2013. 'Investigating the Need of Triggering the Acquisition for Infant Diffusion MRI: A Quantitative Study Including Bootstrap Statistics'. *Neuroimage* 69 (April): 198–205. https://doi.org/10.1016/j.neuroimage.2012.11.063.

Kozák, Lajos Rudolf, Márta Hegyi, Péter Barsi, and Gábor Rudas. 2009. 'Clonazepam Can Facilitate Sensorimotor Functional MRI Examinations in Status Epilepticus during Sleep'. *Ideggyogyaszti Sz.* 62 (3–4): 130–35.

Kozák, L.R., V. Tóth, P. Barsi, and G. Rudas. 2011. '[Functional magnetic resonance imaging for cortical mapping in epilepsy].' *Ideggyogyaszati szemle* 64 (9–10): 294–99.

Krüger, G., and G. H. Glover. 2001. 'Physiological Noise in Oxygenation-Sensitive Magnetic Resonance Imaging'. *Magnetic Resonance in Medicine* 46 (4): 631–37.

Kundu, Bornali, Amy Penwarden, Joel M. Wood, Thomas A. Gallagher, Matthew J. Andreoli, Jed Voss, Timothy Meier, et al. 2013. 'Association of Functional Magnetic Resonance Imaging Indices with Postoperative Language Outcomes in Patients with Primary Brain Tumors'. *Neurosurgical Focus* 34 (4): E6. https://doi.org/10.3171/2013.2.FOCUS12413.

Lee, M. H., C. D. Smyser, and J. S. Shimony. 2013. 'Resting-State FMRI: A Review of Methods and Clinical Applications'. *American Journal of Neuroradiology* 34 (10): 1866–72. https://doi.org/10.3174/ajnr.A3263.

Limotai, Chusak, and Seyed M. Mirsattari. 2012. 'Role of Functional MRI in Presurgical Evaluation of Memory Function in Temporal Lobe Epilepsy'. *Epilepsy Research and Treatment* 2012: 1–12. https://doi.org/10.1155/2012/687219.

Loenneker, Thomas, Franciszek Hennel, and Jürgen Hennig. 1996. 'Multislice Interleaved Excitation Cycles (MUSIC): An Efficient Gradient-Echo Technique for Functional MRI'. *Magnetic Resonance in Medicine* 35 (6): 870–74. https://doi.org/10.1002/mrm.1910350613.

Logothetis, Nikos K., Jon Pauls, Mark Augath, Torsten Trinath, and Axel Oeltermann. 2001. 'Neurophysiological Investigation of the Basis of the FMRI Signal'. *Nature* 412 (6843): 150. https://doi.org/10.1038/35084005.

Lutti, Antoine, David L. Thomas, Chloe Hutton, and Nikolaus Weiskopf. 2013. 'High-Resolution Functional MRI at 3 T: 3D/2D Echo-Planar Imaging with Optimized Physiological Noise Correction: High-Resolution FMRI at 3T'. *Magnetic Resonance in Medicine* 69 (6): 1657–64. https://doi.org/10.1002/mrm.24398.

Markl, Michael, and Jochen Leupold. 2012. ‘Gradient Echo Imaging’. *Journal of Magnetic Resonance Imaging* 35 (6): 1274–89. https://doi.org/10.1002/jmri.23638.

Meszlényi, Regina J., Petra Hermann, Krisztian Buza, Viktor Gál, and Zoltán Vidnyánszky. 2017. ‘Resting State FMRI Functional Connectivity Analysis Using Dynamic Time Warping’. *Frontiers in Neuroscience* 11 (February). https://doi.org/10.3389/fnins.2017.00075.

Moeller, Steen, Essa Yacoub, Cheryl A. Olman, Edward Auerbach, John Strupp, Noam Harel, and Kâmil Uğurbil. 2010. ‘Multiband Multislice GE-EPI at 7 Tesla, with 16-Fold Acceleration Using Partial Parallel Imaging with Application to High Spatial and Temporal Whole-Brain FMRI’. *Magnetic Resonance in Medicine* 63 (5): 1144–53. https://doi.org/10.1002/mrm.22361.

‘MRI Physics: MRI Pulse Sequences - XRayPhysics’. n.d. Accessed 29 March 2019. http://xrayphysics.com/sequences.html.

Nunes, R.G., J.V. Hajnal, X Golay, and D.J. Larkman. 2006. ‘Simultaneous Slice Excitation and Reconstruction for Single Shot EPI’. ISMRM.

Ogawa, S., T. M. Lee, A. S. Nayak, and P. Glynn. 1990. ‘Oxygenation-Sensitive Contrast in Magnetic Resonance Image of Rodent Brain at High Magnetic Fields’. *Magnetic Resonance in Medicine* 14 (1): 68–78.

Ogawa, S., R. S. Menon, D. W. Tank, S. G. Kim, H. Merkle, J. M. Ellermann, and K. Ugurbil. 1993. ‘Functional Brain Mapping by Blood Oxygenation Level-Dependent Contrast Magnetic Resonance Imaging. A Comparison of Signal Characteristics with a Biophysical Model’. *Biophysical Journal* 64 (3): 803–12. https://doi.org/10.1016/S0006-3495(93)81441-3.

Peck, Kyung K., Michelle Bradbury, Nicole Petrovich, Bob L. Hou, Nicole Ishill, Cameron Brennan, Viviane Tabar, and Andrei I. Holodny. 2009. ‘Presurgical Evaluation of Language Using Functional Magnetic Resonance Imaging in Brain Tumor Patients with Previous Surgery’. *Neurosurgery* 64 (4): 644–53. https://doi.org/10.1227/01.NEU.0000339122.01957.0A.

Perlbarg, Vincent, Pierre Bellec, Jean-Luc Anton, Mélanie Pélégrini-Issac, Julien Doyon, and Habib Benali. 2007. ‘CORSICA: Correction of Structured Noise in

FMRI by Automatic Identification of ICA Components'. *Magnetic Resonance Imaging* 25 (1): 35–46. https://doi.org/10.1016/j.mri.2006.09.042.

Petrella, Jeffrey R., Lubdha M. Shah, Katy M. Harris, Allen H. Friedman, Timothy M. George, John H. Sampson, Joseph S. Pekala, and James T. Voyvodic. 2006. 'Preoperative Functional MR Imaging Localization of Language and Motor Areas: Effect on Therapeutic Decision Making in Patients with Potentially Resectable Brain Tumors'. *Radiology* 240 (3): 793–802. https://doi.org/10.1148/radiol.2403051153.

Pillai, J.J. 2010. 'The Evolution of Clinical Functional Imaging during the Past 2 Decades and Its Current Impact on Neurosurgical Planning'. *American Journal of Neuroradiology* 31 (2): 219–25. https://doi.org/10.3174/ajnr.A1845.

Polimeni, Jonathan R., Himanshu Bhat, Thomas Witzel, Thomas Benner, Thorsten Feiweier, Souheil J. Inati, Ville Renvall, Keith Heberlein, and Lawrence L. Wald. 2016. 'Reducing Sensitivity Losses Due to Respiration and Motion in Accelerated Echo Planar Imaging by Reordering the Autocalibration Data Acquisition: Reducing Losses in Accelerated EPI with FLEET-ACS'. *Magnetic Resonance in Medicine* 75 (2): 665–79. https://doi.org/10.1002/mrm.25628.

Polzehl, Jörg, Henning U. Voss, and Karsten Tabelow. 2010. 'Structural Adaptive Segmentation for Statistical Parametric Mapping'. *NeuroImage* 52 (2): 515–23. https://doi.org/10.1016/j.neuroimage.2010.04.241.

Poustchi-Amin, M., S. A. Mirowitz, J. J. Brown, R. C. McKinstry, and T. Li. 2001. 'Principles and Applications of Echo-Planar Imaging: A Review for the General Radiologist'. *Radiographics: A Review Publication of the Radiological Society of North America, Inc* 21 (3): 767–79. https://doi.org/10.1148/radiographics.21.3.g01ma23767.

Pruessmann, Klaas P., Markus Weiger, Markus B. Scheidegger, and Peter Boesiger. 1999. 'SENSE: Sensitivity Encoding for Fast MRI'. *Magnetic Resonance in Medicine* 42 (5): 952–62. https://doi.org/10.1002/(SICI)1522-2594(199911)42:5<952::AID-MRM16>3.0.CO;2-S.

Raj, D., A. W. Anderson, and J. C. Gore. 2001. 'Respiratory Effects in Human Functional Magnetic Resonance Imaging Due to Bulk Susceptibility Changes'. *Physics in Medicine and Biology* 46 (12): 3331–40.

Rangaprakash, D., Michael N. Dretsch, Wenjing Yan, Jeffrey S. Katz, Thomas S. Denney, and Gopikrishna Deshpande. 2017. 'Hemodynamic Response Function Parameters Obtained from Resting-State Functional MRI Data in Soldiers with Trauma'. *Data in Brief* 14 (October): 558–62. https://doi.org/10.1016/j.dib.2017.07.072.

'Retrospective Estimation and Correction of Physiological Fluctuation in Functional MRI - Hu - 1995 - Magnetic Resonance in Medicine - Wiley Online Library'. n.d. Accessed 1 April 2019. https://onlinelibrary.wiley.com/doi/10.1002/mrm.1910340211.

'ReviseMRI.Com : Echo Planar Imaging'. n.d. Accessed 29 March 2019. http://www.revisemri.com/questions/pulse_sequences/epi.

Rossion, Bruno, Katrien Torfs, Corentin Jacques, and Joan Liu-Shuang. 2015. 'Fast Periodic Presentation of Natural Images Reveals a Robust Face-Selective Electrophysiological Response in the Human Brain'. *Journal of Vision* 15 (1): 18–18. https://doi.org/10.1167/15.1.18.

Sahib, Ashish Kaul, Michael Erb, Justus Marquetand, Pascal Martin, Adham Elshahabi, Silke Klamer, Serge Vulliemoz, Klaus Scheffler, Thomas Ethofer, and Niels K. Focke. 2018. 'Evaluating the Impact of Fast-FMRI on Dynamic Functional Connectivity in an Event-Based Paradigm'. *PLOS ONE* 13 (1): e0190480. https://doi.org/10.1371/journal.pone.0190480.

Sahib, Ashish Kaul, Klaus Mathiak, Michael Erb, Adham Elshahabi, Silke Klamer, Klaus Scheffler, Niels K Focke, and Thomas Ethofer. 2016. 'Effect of Temporal Resolution and Serial Autocorrelations in Event-Related Functional MRI: Temporal Resolution and Autocorrelations in FMRI'. *Magnetic Resonance in Medicine* 76 (6): 1805–13. https://doi.org/10.1002/mrm.26073.

Salimi-Khorshidi, Gholamreza, Gwenaëlle Douaud, Christian F. Beckmann, Matthew F. Glasser, Ludovica Griffanti, and Stephen M. Smith. 2014. 'Automatic Denoising of Functional MRI Data: Combining Independent Component Analysis and Hierarchical Fusion of Classifiers'. *NeuroImage* 90 (April): 449–68. https://doi.org/10.1016/j.neuroimage.2013.11.046.

Särkkä, Simo, Arno Solin, Aapo Nummenmaa, Aki Vehtari, Toni Auranen, Simo Vanni, and Fa-Hsuan Lin. 2012. 'Dynamic Retrospective Filtering of

Physiological Noise in BOLD FMRI: DRIFTER'. *NeuroImage* 60 (2): 1517–27. https://doi.org/10.1016/j.neuroimage.2012.01.067.

Setsompop, K., J. Cohen-Adad, B. A. Gagoski, T. Raij, A. Yendiki, B. Keil, V. J. Wedeen, and L. L. Wald. 2012. 'Improving Diffusion MRI Using Simultaneous Multi-Slice Echo Planar Imaging'. *NeuroImage* 63 (1): 569–80. https://doi.org/10.1016/j.neuroimage.2012.06.033.

Setsompop, Kawin, Borjan A. Gagoski, Jonathan R. Polimeni, Thomas Witzel, Van J. Wedeen, and Lawrence L. Wald. 2012. 'Blipped-Controlled Aliasing in Parallel Imaging for Simultaneous Multislice Echo Planar Imaging with Reduced g-Factor Penalty'. *Magnetic Resonance in Medicine* 67 (5): 1210–24. https://doi.org/10.1002/mrm.23097.

Smith, Stephen M., Karla L. Miller, Steen Moeller, Junqian Xu, Edward J. Auerbach, Mark W. Woolrich, Christian F. Beckmann, et al. 2012. 'Temporally-Independent Functional Modes of Spontaneous Brain Activity'. *Proceedings of the National Academy of Sciences of the United States of America* 109 (8): 3131–36. https://doi.org/10.1073/pnas.1121329109.

Smith, Stephen M, Diego Vidaurre, Christian F Beckmann, Matthew F Glasser, Mark Jenkinson, Karla L Miller, Thomas E Nichols, et al. 2013. 'Functional Connectomics from Resting-State FMRI'. *Trends in Cognitive Sciences* 17 (12): 666–82. https://doi.org/10.1016/j.tics.2013.09.016.

Sodickson, Daniel K., and Warren J. Manning. 1997. 'Simultaneous Acquisition of Spatial Harmonics (SMASH): Fast Imaging with Radiofrequency Coil Arrays'. *Magnetic Resonance in Medicine* 38 (4): 591–603. https://doi.org/10.1002/mrm.1910380414.

Thomas, Christopher G., Richard A. Harshman, and Ravi S. Menon. 2002. 'Noise Reduction in BOLD-Based FMRI Using Component Analysis'. *NeuroImage* 17 (3): 1521–37. https://doi.org/10.1006/nimg.2002.1200.

Todd, Nick, Oliver Josephs, Peter Zeidman, Guillaume Flandin, Steen Moeller, and Nikolaus Weiskopf. 2017. 'Functional Sensitivity of 2D Simultaneous Multi-Slice Echo-Planar Imaging: Effects of Acceleration on g-Factor and Physiological Noise'. *Frontiers in Neuroscience* 11 (March). https://doi.org/10.3389/fnins.2017.00158.

Todd, Nick, Steen Moeller, Edward J. Auerbach, Essa Yacoub, Guillaume Flandin, and Nikolaus Weiskopf. 2016. 'Evaluation of 2D Multiband EPI Imaging for High-Resolution, Whole-Brain, Task-Based FMRI Studies at 3T: Sensitivity and Slice Leakage Artifacts'. *NeuroImage* 124 (January): 32–42. https://doi.org/10.1016/j.neuroimage.2015.08.056.

Tong, Yunjie, Lia M. Hocke, and Blaise deB. Frederick. 2014. 'Short Repetition Time Multiband Echo-Planar Imaging with Simultaneous Pulse Recording Allows Dynamic Imaging of the Cardiac Pulsation Signal: Dynamic Imaging of the Cardiac Pulsation Signal'. *Magnetic Resonance in Medicine* 72 (5): 1268–76. https://doi.org/10.1002/mrm.25041.

Triantafyllou, Christina, Lawrence L. Wald, and Richard D. Hoge. 2011. 'Echo-Time and Field Strength Dependence of BOLD Reactivity in Veins and Parenchyma Using Flow-Normalized Hypercapnic Manipulation'. *PLOS ONE* 6 (9): e24519. https://doi.org/10.1371/journal.pone.0024519.

Verstynen, Timothy D., and Vibhas Deshpande. 2011. 'Using Pulse Oximetry to Account for High and Low Frequency Physiological Artifacts in the BOLD Signal'. *NeuroImage* 55 (4): 1633–44. https://doi.org/10.1016/j.neuroimage.2010.11.090.

Vikingstad, Eric M., Yue Cao, Ajith J. Thomas, Alex F. Johnson, Ghaus M. Malik, and Kenneth M. A. Welch. 2000. 'Language Hemispheric Dominance in Patients with Congenital Lesions of Eloquent Brain': *Neurosurgery* 47 (3): 562–70. https://doi.org/10.1227/00006123-200009000-00004.

Wengenroth, Martina, M. Blatow, J. Guenther, M. Akbar, V. M. Tronnier, and C. Stippich. 2011. 'Diagnostic Benefits of Presurgical FMRI in Patients with Brain Tumours in the Primary Sensorimotor Cortex'. *European Radiology* 21 (7): 1517–25. https://doi.org/10.1007/s00330-011-2067-9.

Windischberger, Christian, Herbert Langenberger, Thomas Sycha, Edda M Tschernko, Gabriele Fuchsjäger-Mayerl, Leopold Schmetterer, and Ewald Moser. 2002. 'On the Origin of Respiratory Artifacts in BOLD-EPI of the Human Brain'. *Magnetic Resonance Imaging* 20 (8): 575–82. https://doi.org/10.1016/S0730-725X(02)00563-5.

Wood, J. M., B. Kundu, A. Utter, T. A. Gallagher, J. Voss, V. A. Nair, J. S. Kuo, et al. 2011. 'Impact of Brain Tumor Location on Morbidity and Mortality: A Retrospective Functional MR Imaging Study'. *American Journal of Neuroradiology* 32 (8): 1420–25. https://doi.org/10.3174/ajnr.A2679.

Worsley, K. J., and K. J. Friston. 1995. 'Analysis of FMRI Time-Series Revisited--Again'. *NeuroImage* 2 (3): 173–81. https://doi.org/10.1006/nimg.1995.1023.

Wu, D. H., J. S. Lewin, and J. L. Duerk. 1997. 'Inadequacy of Motion Correction Algorithms in Functional MRI: Role of Susceptibility-Induced Artifacts'. *Journal of Magnetic Resonance Imaging: JMRI* 7 (2): 365–70.

Zahneisen, Benjamin, Jakob Assländer, Pierre LeVan, Thimo Hugger, Marco Reisert, Thomas Ernst, and Jürgen Hennig. 2014. 'Quantification and Correction of Respiration Induced Dynamic Field Map Changes in FMRI Using 3D Single Shot Techniques'. *Magnetic Resonance in Medicine* 71 (3): 1093–1102. https://doi.org/10.1002/mrm.24771.

9. Publications

Publications related to the thesis

1. Kiss M., Hermann P., Vidnyánszky Z., Gál V.: Reducing task-based fMRI scanning time using simultaneous multislice echo planar imaging. Neuroradiology (2018) Mar;60(3):293-302. **IF: 2.504**
2. Kiss M., Gál A.V., Kozák LR, Martos J., Nagy Z.: Fiziológiai műtermékek jelentősége az idegsebészeti műtétek előtt végzett funkcionális MR vizsgálatokban. Ideggyógyászati Szemle **IF: 0.252**
3. M. Kiss, J. Martos, VA Gál: Physiological artefacts correction technique at pre-surgical task-related functional MRI. http://dx.doi.org/10.1594/ecr2017/C-0351

Publications unrelated to the thesis

1. Kovács A., Kiss M., Pintér N., Szirmai I., Kamondi A.: Characteristics of Tremor Induced by Lesions of the Cerebellum. The Cerebellum (2019) 18:705. **IF: 3.41**

2. Horvath A., Kiss M., Szucs A., Kamondi A.: Precuneus-Dominant Degeneration of Parietal Lobe Is at Risk of Epilepsy in Mild Alzheimer's Disease. Front. Neurol., 22 August 2019. **IF: 2.635**

3. M. Kiss, G. Rudas, LR Kozak: The outcome of fMRI language mapping is affected by patient fatigue. http://dx.doi.org/10.1594/ecr2016/C-2314

4. A Lakatos, M. Kiss, S. Shaikh., B. Lombay: Radiation dose reduction in pediatric CT examinations. http://dx.doi.org/10.1594/ecr2012/C-1637

5. M. Kiss, J. Martos, P. Várallyay, V.A. Gál: Arterial Spin Labeling – basics, clinical applications and pitfalls. http://dx.doi.org/10.1594/ecr2017/C-1600

6. M. Kiss, J. Martos, LR Kozak, B. Lombay: Can we avoid the traps at 3T MRI? http://dx.doi.org/10.1594/ecr2015/C-1473

7. Kiss M., Lakatos A., Lombay B.: A sugárdózis csökkentés lehetőségei gyermekek CT-vizsgálatánál. Magyar Radiológia Online 3. évfolyam 2012/12

8. Martos J., Kiss M.: A funkcionális MR vizsgálatok új diagnosztikai lehetőségei 3 Teslás készülék segítségével. IME XIV. évfolyam, 2015/8; 53-57.

9. Sirokai B., Kiss M., Kovacs L., Benyo B., Benyo Z., Haidegger T.: Best Practices in Electromagnetic Tracking System Assessment. II. SCATh Joint Workshop on New Technologies for Computer/Robot Assisted Surgery.2012 ISBN:978-94-6018-549-6

10. M. Kiss, Á. Kettinger, Z. Vidnyánszky, V. Gál: Simultaneous multislice fMRI improves the physiological noise removal in resting-state fMRI. Fifth Biennial Conference on Resting State and Brain Connectivity 2016, Vienna, Austria

11. M. Kiss, G. Rudas, LR Kozák: Neural Correlates of possible mind wandering and attentional compensation during extended fMRI sessions. ESMRMB 206; 33rd Annual scientific meeting.

10. Acknowledgement

First of all, I would like to thank my supervisor Lajos Rudolf Kozák for teaching me the basics of neuroscience research, his continuous support, effort and for the patience. I am tremendously grateful Viktor Gál for technical support of my research and for entrusting me with his insights and long term vision of functional MRI data analysis.

Special thanks must be paid to Prof. Zoltán Vidnyánszky, his research group to provide an opportunity to learn the basics of neuroscience. I am also thankful to all my colleagues in our lab, who also became my friends.

Special thanks must be paid Prof. Zoltán Nagy for all his questions and advices and for many conversations about the research.

My most special thanks to my family, especially Kitti and Lili, for their continuous emotional support, encouragement, understanding and for their patience.

Last, but not least I would like to thank Prof. Béla Lombay and János Martos for the last 15 years.